

CHAPTER 4

RESULTS AND DISCUSSION (PART I):

LEAD MAGNESIUM NIOBATE

In this chapter, the results are presented of the investigation of both powder and ceramic forms of lead magnesium niobate (PMN) which is one of the two end components of the PMN-PT system. Phase formation-structure-property relationships are brought out for this PMN component, and discussed in terms of phase formation, microstructure, dielectric properties and thermal expansion. Therefore, it is appropriate to focus initially on the synthesis of PMN powders via the *B*-site precursor techniques [28,38,39], before embarking on the fabrication of PMN ceramics.

4.1 Magnesium Niobate Powders

In this work, a *B*-site mixed oxide synthetic route for preparing high purity PMN powders has been developed. To ensure a single-phase perovskite formation, intermediate phases of MgNb_2O_6 (columbite) and $\text{Mg}_4\text{Nb}_2\text{O}_9$ (corundum) were separately employed as starting precursor. Both intermediate phases are obtained via a well-known mixed oxide route advocated by Swartz *et al.* [28] and Lu *et al.* [39], respectively. The development of $\text{Mg}_4\text{Nb}_2\text{O}_9$ powders (corundum), to date, has not been as extensive as that of MgNb_2O_6 . Only limited attempts have been made to improve the yield of $\text{Mg}_4\text{Nb}_2\text{O}_9$ powders derived from the solid-state reaction by optimizing milling method or calcination condition [142,143]. Moreover, the optimization of a combination between the milling method and the calcination in the mixed oxide process has not been studied. Therefore, as an extension of earlier works

on the preparation of $\text{Mg}_4\text{Nb}_2\text{O}_9$ powders [33,142], the purpose of this section is to explore a simple mixed oxide synthetic route for the production of $\text{Mg}_4\text{Nb}_2\text{O}_9$ powders and compare the characteristics of the resulting powder. Two milling techniques were employed as the mixing method. A conventional ball milling was compared against a rapid vibro-milling in terms of their phase formation, particle size, morphology and microchemical compositions of the powders calcined at various conditions.

TG and DTA results for the mixture of MgO and Nb_2O_5 milled by both methods are shown in Figs. 4.1 and 4.2, respectively. In general, similar trend of thermal characteristics is observed in both precursors. As shown in Fig. 4.1, the precursors prepared with both milling methods exhibit two distinct weight losses below 600°C . The first weight loss occurs below 200°C and the second one above 250°C . In the temperature range from room temperature to $\sim 150^\circ\text{C}$, both samples show small exothermic peaks in the DTA curves at $\sim 120^\circ\text{C}$ (Fig. 4.2), which are related to the first weight loss. These DTA peaks can be attributed to the decomposition of the organic species such as rubber lining from the milling process similar to the reported earlier [142]. In comparison between the two milling methods, after the first weight loss, the ball-milling precursor (solid line) shows a slightly less weight loss over the temperature range of $\sim 150\text{-}250^\circ\text{C}$, followed by a much more sharp fall in specimen weight with increasing temperature from $\sim 250\text{-}500^\circ\text{C}$. This precursor also exhibits a significantly larger overall weight loss ($\sim 7.25\%$) than that of the vibro-milling ($\sim 1.50\%$). This may be accounted for by the fact that the vibro-milling method provides faster size reduction rate and is able to enhance mixing

capability with lower contamination possibility due to shorter milling time applied as suggested by several authors [40,144,145].

Corresponding to the second fall in specimen weight, by increasing the temperature up to ~ 700 °C, the solid-state reaction occurs between magnesium oxide and niobium oxide. The broad exothermic characteristic in both DTA curves represents that reaction, which has a maximum at ~ 550 and 620 °C for ball-milling and vibro-milling precursors, respectively. No significant weight loss was observed for the temperatures above 800 °C in the TG curves (Fig. 4.1), indicating that the minimum firing temperature to obtain MgO-Nb₂O₅ compounds is in good agreement with XRD results (Figs. 4.3 and 4.4) and other workers [38,40,146]. However, the DTA curves show that there are other small peaks with maximum at ~ 1080 °C (for ball-milling) and 1050 °C (for vibro-milling). It is to be noted that there is no obvious interpretation of these peaks, although it is likely to correspond to a phase transition reported by a number of workers [147,148]. The different temperature, intensities, and shapes of the thermal peaks for the two precursors are probably related to the different milling conditions between the two methods, and consequently caused by the removal of organic species (such as rubber lining) and reactivity of species differently milled (difference in size and size distribution) and mixed in the powders. These data were used to define the range of temperatures for XRD investigation to between 550 and 1100 °C.

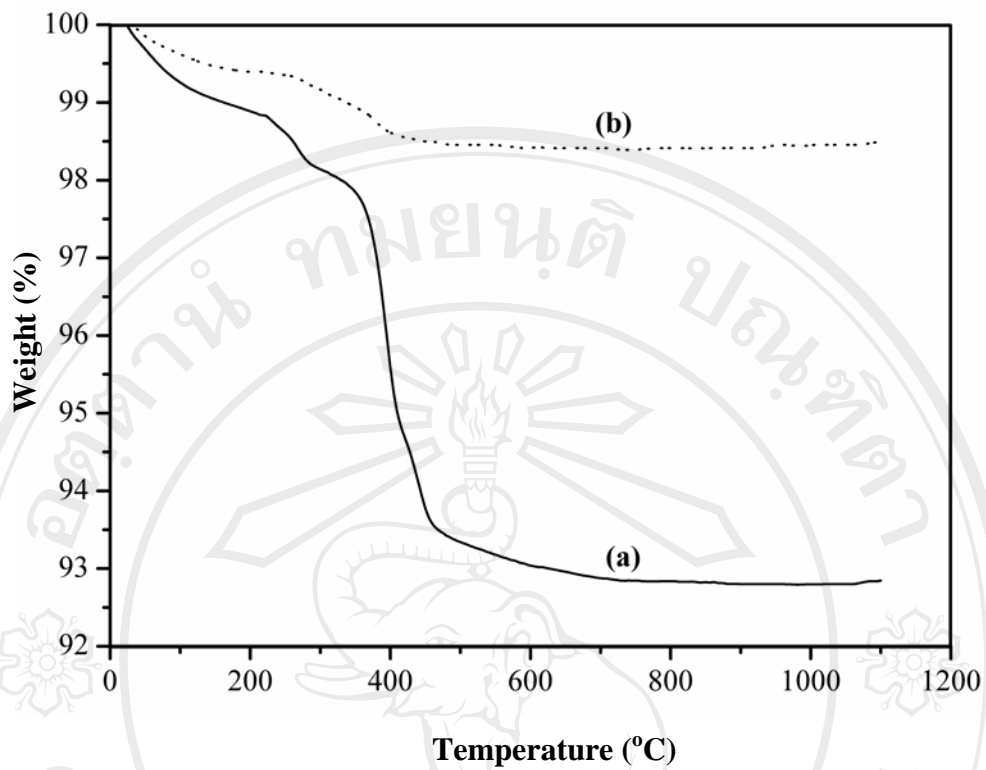


Fig. 4.1 TG curves of the two MgO-Nb₂O₅ mixtures derived from (a) ball-milling and (b) vibro-milling methods.

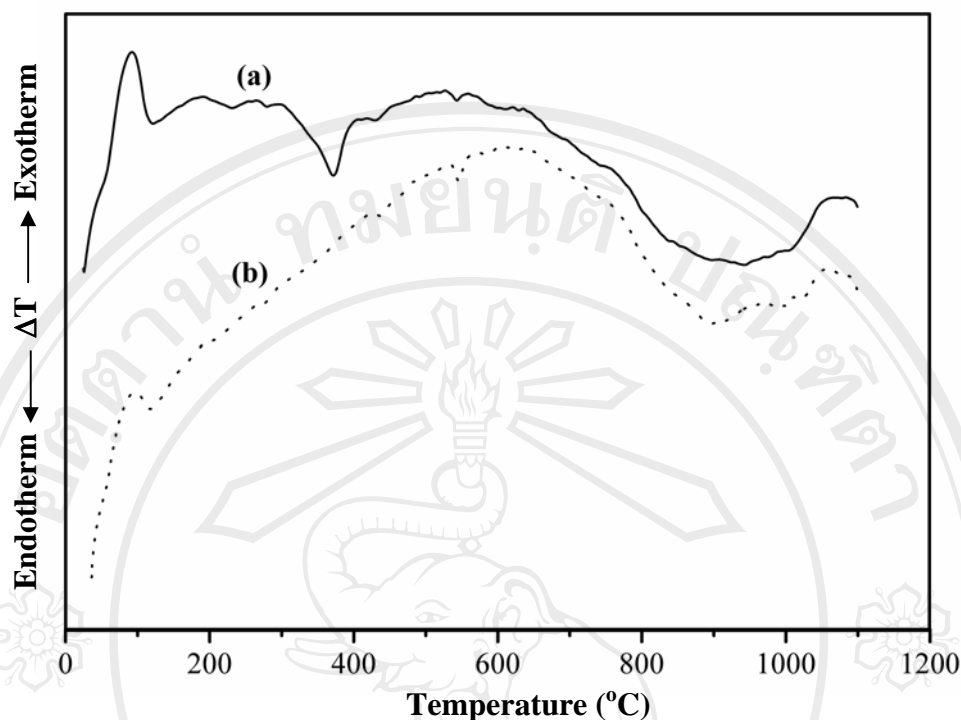


Fig. 4.2 DTA curves of the two MgO-Nb₂O₅ mixtures derived from (a) ball-milling and (b) vibro-milling methods

To further study the phase development with increasing calcination temperature in each of the two precursors, they were calcined for 2 h in air with constant heating/cooling rates of 10 °C/min at various temperatures, up to 1100 °C, followed by phase analysis using XRD. As shown in Figs. 4.3 and 4.4, for the powders calcined at 550 °C, only X-ray peaks of MgO and Nb₂O₅ are present, indicating that the elimination of organic species occurs below 500 °C, which agrees with the TG-DTA results determined previously. The strongest reflections of the mixed phases of MgO (●) and Nb₂O₅ (○) can be correlated with ICDD file nos. 71-1176 [149] and 28-317 [150], respectively.

From Figs. 4.3 and 4.4, it is seen that little crystalline phase of MgNb_2O_6 (∇), earlier reported by many researchers [38,148,151] was found at 600 °C as separated phases in both calcined powders. This MgNb_2O_6 phase (ICDD file no. 33-875 [152]) has a columbite-type structure with an orthorhombic unit cell ($a = 5.70 \text{ \AA}$, $b = 14.19 \text{ \AA}$ and $c = 5.032 \text{ \AA}$) with space group $I41/amd$ (no. 141), in agreement with literature [142,154]. As the temperature increased to 700 °C, the intensity of the MgNb_2O_6 peaks in both calcined powders was further enhanced and became the predominant phase, in consistent with the TG-DTA results. From Figs. 4.3 and 4.4, it is seen that the peaks corresponding to MgO and Nb_2O_5 phases were completely eliminated after calcination at 800 °C in both powders. These observations are associated to the DTA peaks found at the same temperature range within the broad exothermic effects (Fig. 4.2). After calcination at 850 °C, some new peaks (\blacktriangledown) of the desired $\text{Mg}_4\text{Nb}_2\text{O}_9$ started to appear, mixing with MgNb_2O_6 and MgO phases in both powders, in consistent with literature [142]. To a first approximation, this $\text{Mg}_4\text{Nb}_2\text{O}_9$ phase (ICDD file no. 38-1459 [153]) has a corundum-type structure with a hexagonal unit cell ($a = 5.162 \text{ \AA}$ and $c = 14.024 \text{ \AA}$) with space group (no. 165), in consistent with other researchers [142,154].

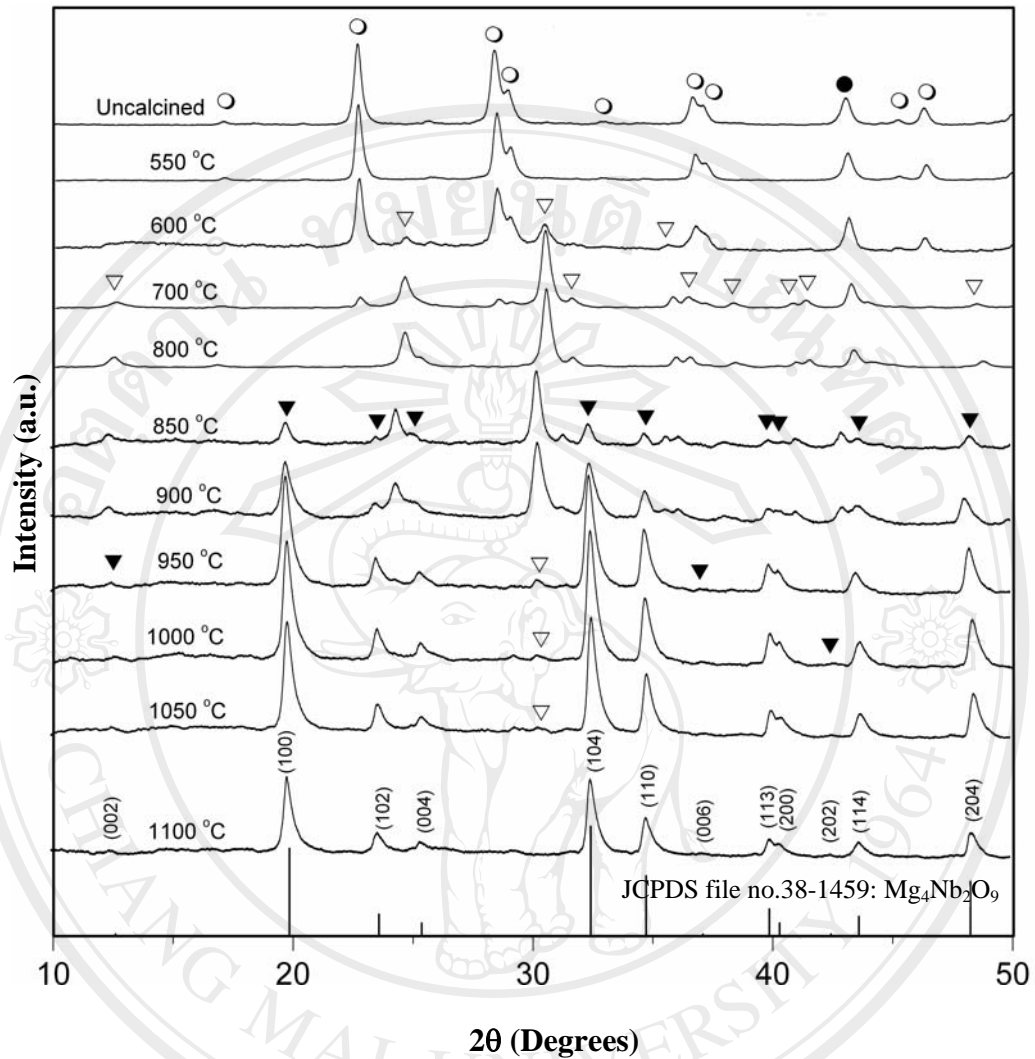


Fig. 4.3 Powder XRD patterns of the ball-milling $\text{Mg}_4\text{Nb}_2\text{O}_9$ powders calcined at various conditions for 2 h with constant heating/cooling rates of $10\text{ }^\circ\text{C}/\text{min}$ (● MgO , ○ Nb_2O_5 , ▽ MgNb_2O_6 and ▼ $\text{Mg}_4\text{Nb}_2\text{O}_9$).

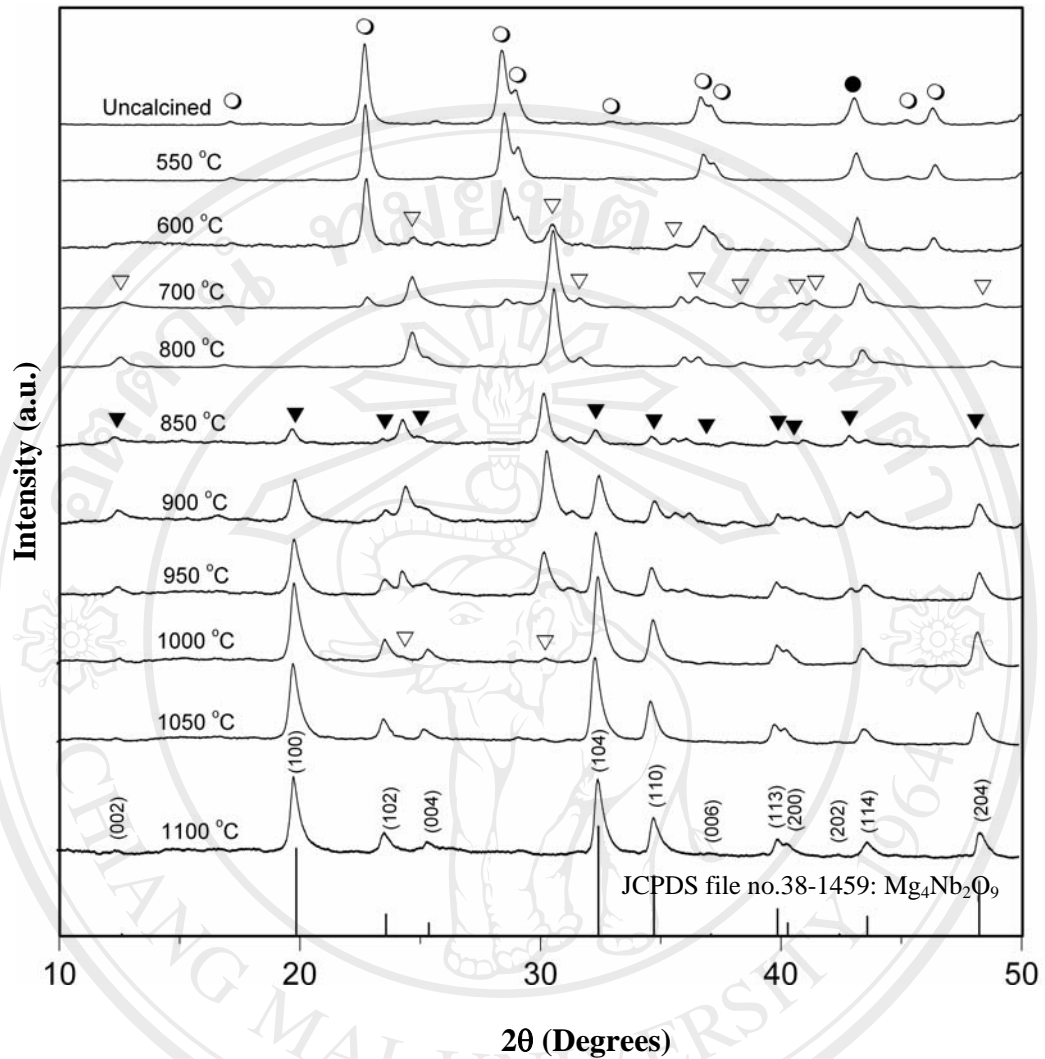


Fig. 4.4 Powder XRD patterns of the vibro-milling $\text{Mg}_4\text{Nb}_2\text{O}_9$ powders calcined at various conditions for 2 h with constant heating/cooling rates of $10\text{ }^\circ\text{C}/\text{min}$ (● MgO , ○ Nb_2O_5 , ▽ MgNb_2O_6 and ▼ $\text{Mg}_4\text{Nb}_2\text{O}_9$).

Upon calcination at 1100 °C, the major phase of $\text{Mg}_4\text{Nb}_2\text{O}_9$ has been clearly identified in the ball-milling powders and most of second phases were eliminated. In particular, the peaks corresponding to MgNb_2O_6 disappeared. However, in comparison, a single-phase of $\text{Mg}_4\text{Nb}_2\text{O}_9$ is already formed when the vibro-milling precursor was calcined at 1050 °C. Apart from calcination temperatures, the effect of dwell time was also found to be significant (Figs. 4.5 and 4.6). It is seen that an essentially monophasic $\text{Mg}_4\text{Nb}_2\text{O}_9$ of corundum structure is obtainable in the ball-milling powders when the dwell time was extended to 5 h at 1050 °C (Fig. 4.5), which is 3 h longer than that of the vibro-milling precursor (Fig. 4.6). In this work, an attempt was also made to calcine these powders under various heating/cooling rates (Figs. 4.5(d-f) and 4.6(e-g)). In this connection, it is shown that the yield of $\text{Mg}_4\text{Nb}_2\text{O}_9$ phase did not vary significantly with different heating/cooling rates ranging from 10 to 30 °C/min, in good agreement with earlier results reported by earlier work [142] for the mixture of the two kinds of refractory oxides.

The amount of corundum phase present in each of the powders was estimated using Eq. (3.9) (see section 3.2.2). It should be seen as a first approximation since its applicability requires comparable maximum intensities of the peaks of major and minor phases. For the purpose of estimating the concentration of the phase present has been applied to the powder XRD patterns obtained as given in Table 4.1.

Table 4.1 Calculated amount of $\text{Mg}_4\text{Nb}_2\text{O}_9$ phase as a function of calcination conditions.

Calcination conditions		Qualitative concentrations of phases [*]			
Temperature (°C)	Dwell time (h)	Ball-milling		Vibro-milling	
		$\text{Mg}_4\text{Nb}_2\text{O}_9$ (wt%)	MgNb_2O_6 (wt%)	$\text{Mg}_4\text{Nb}_2\text{O}_9$ (wt%)	MgNb_2O_6 (wt%)
850	2	20.9	79.1	5.0	95.0
900	2	42.4	57.6	21.3	78.7
950	2	91.2	8.8	58.8	41.2
1000	2	93.7	6.3	93.4	6.6
1050	1	-	-	98.3	1.7
1050	2	93.9	6.0	100	0
1050	3	99.0	1.0	100	0
1050	4	99.1	0.9	100	0
1050	5	100	0	100	0
1100	2	100	0	100	0

^{*}The estimated precision of the concentrations for the two phases is $\pm 0.1\%$

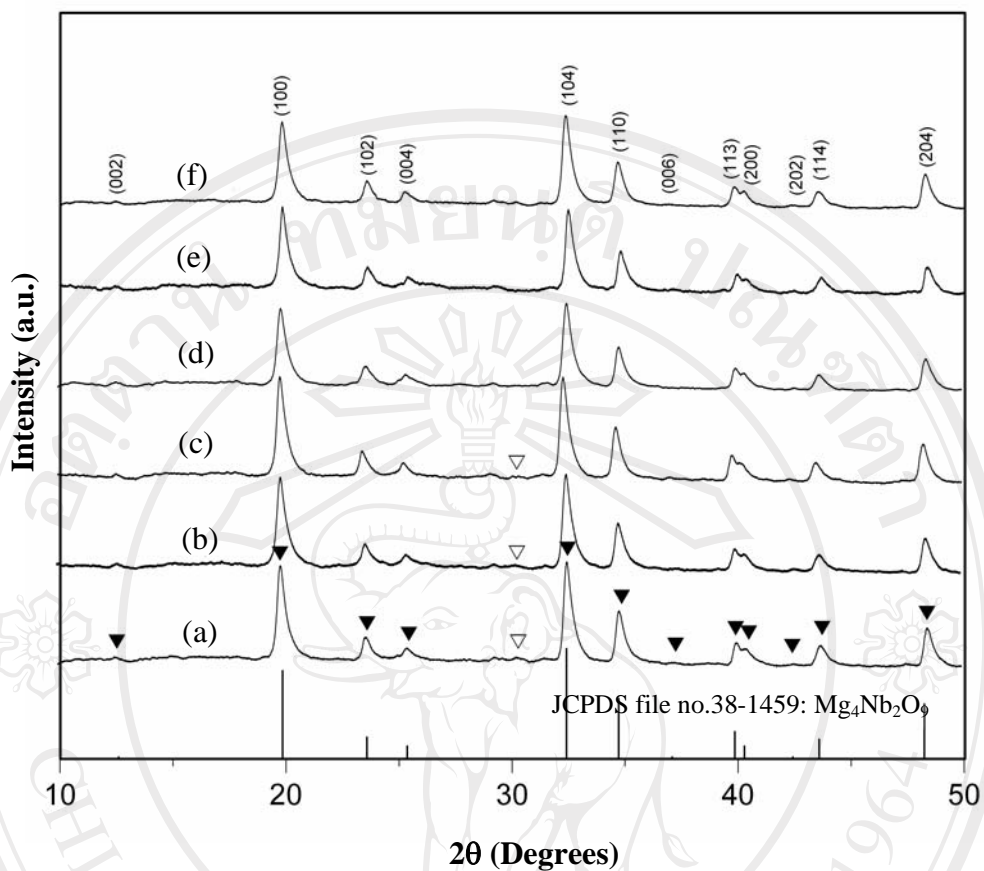


Fig. 4.5 Powder XRD patterns of the ball-milling $\text{Mg}_4\text{Nb}_2\text{O}_9$ powders calcined at $1050\text{ }^\circ\text{C}$ with heating/cooling rates of $10\text{ }^\circ\text{C}/\text{min}$. for (a) 2 h, (b) 3 h, (c) 4 h and (d) 5 h, and at $1050\text{ }^\circ\text{C}$ for 5 h with heating/cooling rates of (e) $20\text{ }^\circ\text{C}/\text{min}$ and (f) $30\text{ }^\circ\text{C}/\text{min}$ (∇ MgNb_2O_6 and \blacktriangledown $\text{Mg}_4\text{Nb}_2\text{O}_9$).

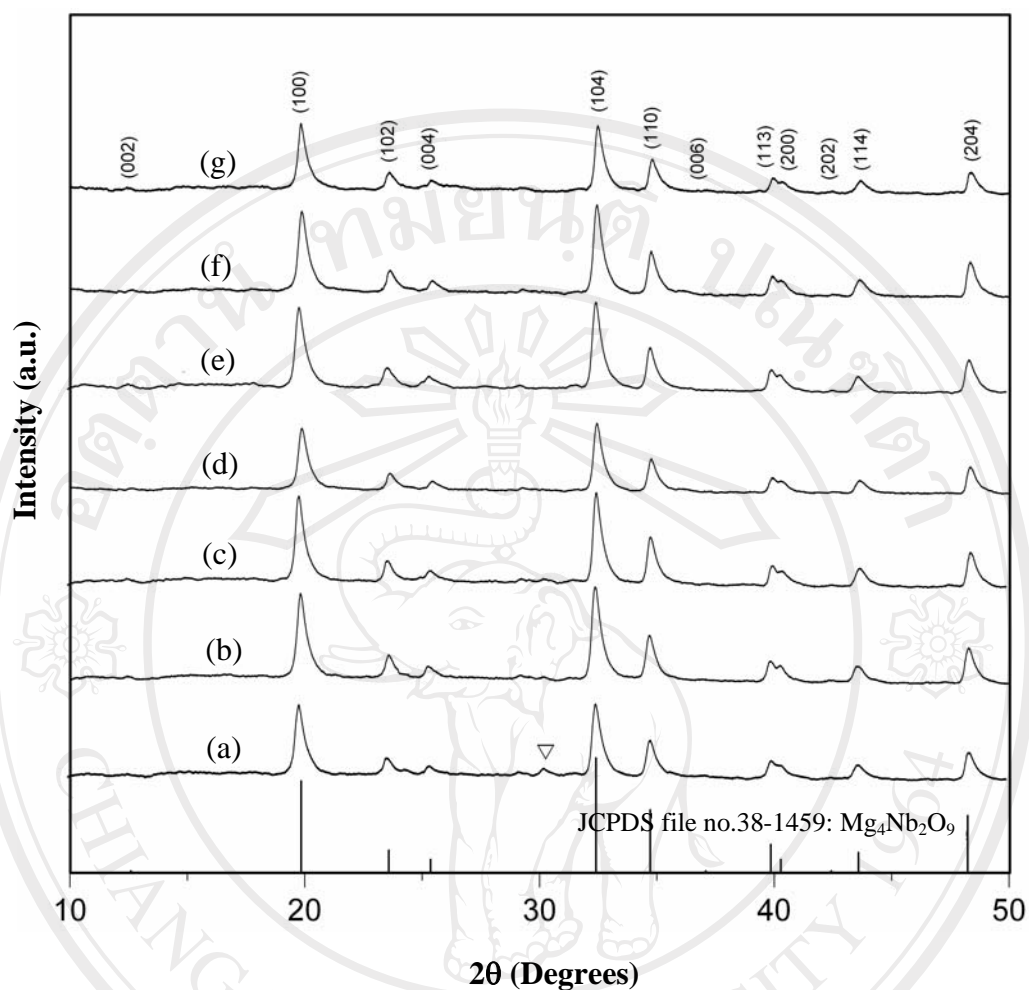


Fig. 4.6 Powder XRD patterns of the vibro-milling $\text{Mg}_4\text{Nb}_2\text{O}_9$ powders calcined at 1050 °C with heating/cooling rates of 10 °C/min for (a) 1 h, (b) 2 h, (c) 3 h, (d) 4 h and (e) 5 h, and at 1050 °C for 5 h with heating/cooling rates of (f) 20 °C/min and (g) 30 °C/min (∇ MgNb_2O_6).

It is well established that the columbite-type MgNb_2O_6 tends to form together with the corundum-type $\text{Mg}_4\text{Nb}_2\text{O}_9$, depending on calcination conditions [142,155]. In the work reported here, evidence for the formation of MgNb_2O_6 phase, which coexists with the $\text{Mg}_4\text{Nb}_2\text{O}_9$ phase, is found after calcination at temperature ~ 850 - 950 °C, similar to those reported by previous works [142,156]. The formation temperature and dwell times for high purity $\text{Mg}_4\text{Nb}_2\text{O}_9$ observed in the powders derived from a combination of a mixed oxide synthetic route and a careful calcination condition (especially with a rapid vibro-milling technique) are slightly lower than those reported for the powders prepared via many other conventional mixed oxide methods [144,154,157].

Based on the DTA and XRD data, it may be concluded that, over a wide range of calcination conditions, single-phase $\text{Mg}_4\text{Nb}_2\text{O}_9$ cannot be straightforwardly formed via a solid-state mixed oxide synthetic route, as verified by a number of researchers [142,147,153]. The experimental work carried out here suggests that the optimal calcination conditions for single-phase $\text{Mg}_4\text{Nb}_2\text{O}_9$ are 1050 °C for 5 h or 1100 °C for 2 h (ball-milling) and 1050 °C for 2 h (vibro-milling), with heating/cooling rates as fast as 30 °C/min. The optimized formation temperature of single-phase $\text{Mg}_4\text{Nb}_2\text{O}_9$ was lower for the vibro-milling method probably due to the higher degree of mixing. Therefore, in general, the methodology presented in this work provides a simple method for preparing corundum $\text{Mg}_4\text{Nb}_2\text{O}_9$ powders via a solid-state mixed oxide synthetic route. It is interesting to note that, by using either ball-milling or vibro-milling methods with its respective optimized calcination condition, the reproducible, lower cost and flexible process involving simple synthetic route can produce high

purity corundum $\text{Mg}_4\text{Nb}_2\text{O}_9$ (with impurities undetected by XRD technique) from relatively impure and inexpensive commercially available raw materials.

SEM micrographs of the calcined $\text{Mg}_4\text{Nb}_2\text{O}_9$ powders derived from ball- and vibro-milling methods are shown in Fig. 4.7 (a) and (b), respectively. In general, the particles are agglomerated and basically irregular in shape, with a substantial variation in particle size. Observed diameters range from 0.52 to 1.41 μm and 0.17 to 1.69 μm for ball- and vibro-milling methods, respectively (Table 4.2). However, it is seen that higher degree of agglomeration with more rounded particle morphology is observed in the powders produced by vibro-milling. The strong inter-particle bond within each aggregate is evidenced by the formation of a well-established necking between neighbouring particles. This observation could be attributed to the mechanism of surface energy reduction of the ultrafine powders, i.e. the smaller the powder the higher the specific surface area [144,145]. In general, it is seen that higher and longer heat treatment of ball-milling powders leads to larger particle sizes with hard agglomeration. The averaged particle size of vibro-milling $\text{Mg}_4\text{Nb}_2\text{O}_9$ powders with finer particle size is regarded as advantage for better reactivity.

A combination of SEM and EDX techniques has demonstrated that an MgO-rich phase (spherical particle with diameter of $\sim 50\text{-}100$ nm) exists neighbouring the $\text{Mg}_4\text{Nb}_2\text{O}_9$ parent phase, as circled in Figs. 4.7 (a) and (b). The existence of discrete nano-sized MgO phase points to the poor reactivity of MgO, although the concentration is too low for detection by XRD in consistent with earlier work [142].

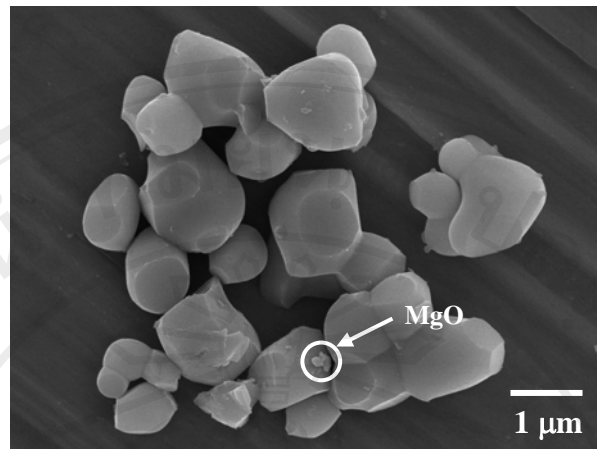
Fig. 4.8 shows the particle size distribution curves of calcined $\text{Mg}_4\text{Nb}_2\text{O}_9$ powders derived from both milling methods. As listed in Table 4.2, the particle size falls within the range of 2.0-4.0 and 0.3-5.5 μm for powders from ball- and vibro-milling

methods, respectively. Even taking into account that the analysis does not reveal the real dimension of single particles (due to agglomeration effects as expected from the SEM results in Fig. 4.7), a uniform frequency distribution curve was observed for the ball-milling powders whilst broad distribution curve with tiny tail at front covering the range of 0.3-0.8 μm in sizes was found for the vibro-milling powders (dashed line), reflecting more of the size of agglomerates than the real size of particles, in good agreement with the SEM results previously determined.

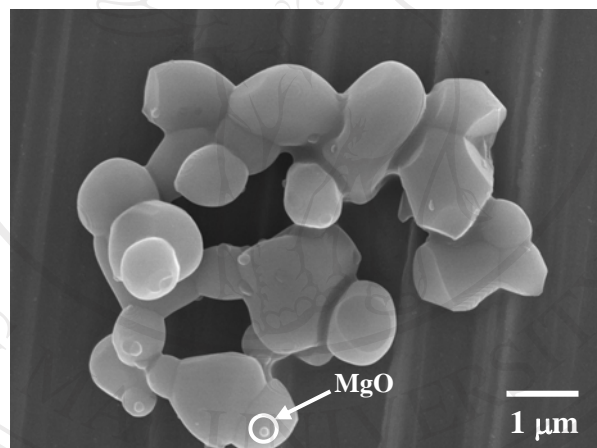
Table 4.2 Particle sizes range of $\text{Mg}_4\text{Nb}_2\text{O}_9$ particles measured by different techniques.

Measurement techniques	Particle size range (average)	
	Ball-milling	Vibro-milling
XRD (nm \pm 2.0) ^a	23.90	23.40
Laser diffraction (μm \pm 0.2)	2.00-4.00 (1.87)	0.30-5.50 (1.54)
SEM (μm \pm 0.1)	0.52-1.41 (0.97)	0.17-1.69 (0.93)
TEM (μm \pm 0.01)	0.01-1.00 (0.53)	0.01-0.03 (0.02)

^a Crystallite size



(a)



(b)

Fig. 4.7 SEM micrographs of the (a) ball-milling and (b) vibro-milling $\text{Mg}_4\text{Nb}_2\text{O}_9$ powders after calcined at their optimal conditions.

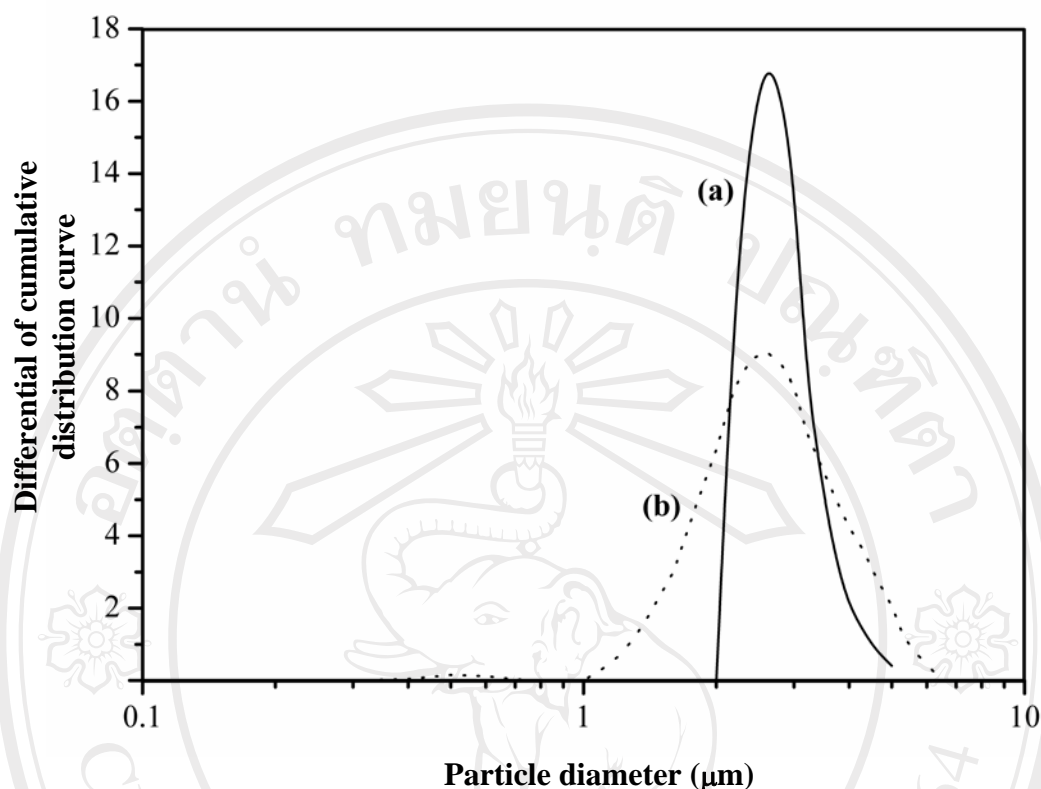


Fig. 4.8 The particle size distribution of (a) ball-milling and (b) vibro-milling $Mg_4Nb_2O_9$ powders after calcined at their optimal conditions.

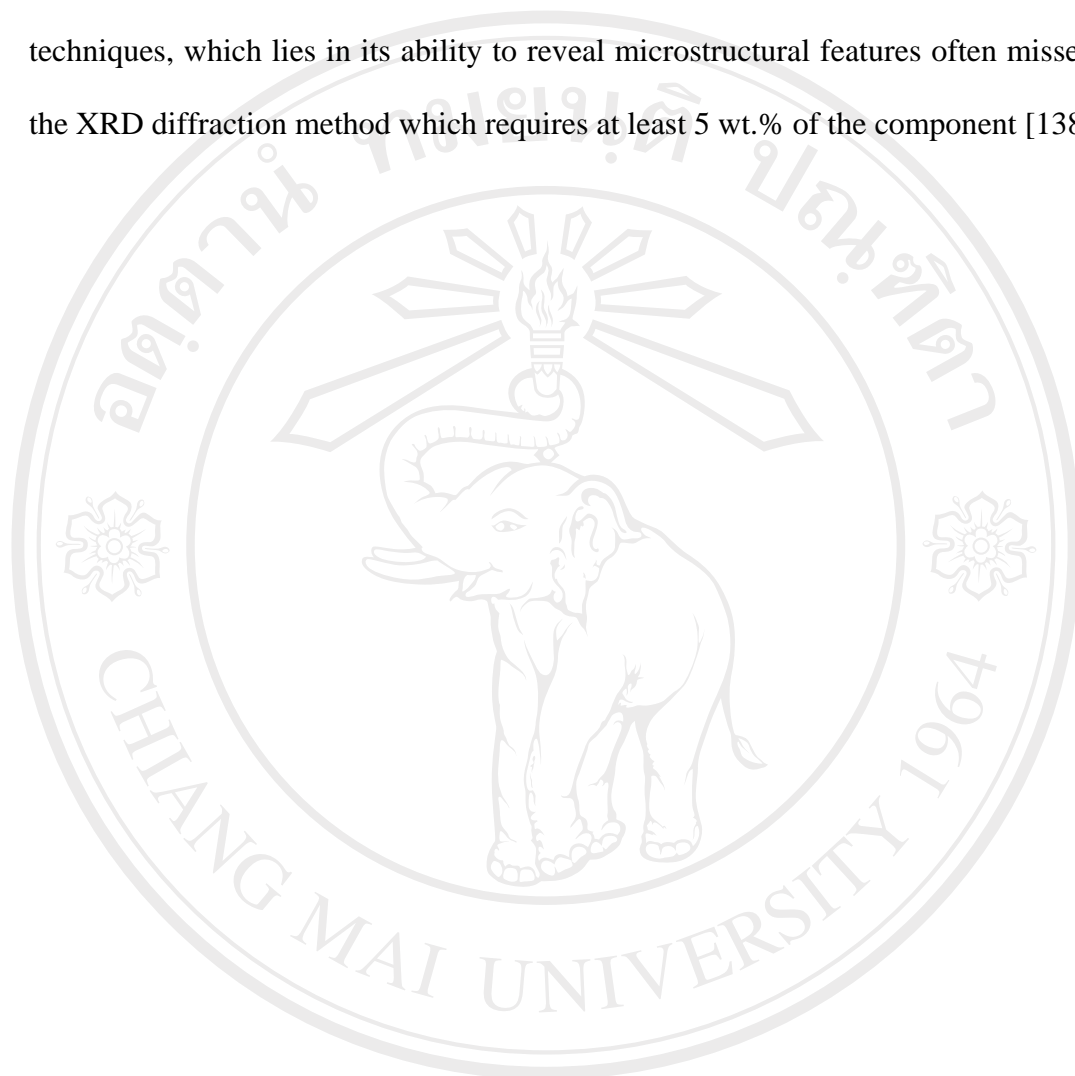
Bright field TEM images of discrete particles of the calcined $Mg_4Nb_2O_9$ powders are shown in Fig. 4.9 (ball-milling) and Fig. 4.10 (vibro-milling), indicating the particle sizes and shapes at higher magnifications. The observed morphology reveals the considerable difference in both size and shapes between the two particles.

Primary particle in vibro-milling powders is clearly smaller in size than the ball-milling powders. As seen in Fig. 4.9 (a), the ball-milling powders consist mainly of irregular round shape primary particles with a diameter of $\sim 1 \mu m$ or less. In addition to the primary particles, the powders have another kind of very fine particle (brighter area) with diameter of about 93 nm (it is referred to as nanoparticle). Only single

nanoparticle can be observed in this TEM micrograph. In contrast, the vibro-milling powders consist mainly of submicrometer-sized primary particles accompanying with several dark and bright areas (Fig. 4.10 (a)). The particle diameters in these TEM micrographs are also given in Table 4.2. It is possible to observe in Table 4.2 that the particle sizes determined by XRD technique have almost the same value in nanometer range for different milling methods. It should be noted that the calculated values from the XRD technique were determined from the XRD peak-broadening and actually present the crystallite sizes, whereas the values from other methods as listed in Table 4.2 represent the particle sizes, which include polycrystalline, agglomerates, defects, etc. [137]. In addition, these other methods also provide information on particle morphology and powder quality, which is not available from the XRD technique alone. Thus the combination of the data listed in Table 4.2 provides better assessment of the powders produced from different milling techniques.

By employing a combination of both selected area electron diffraction (SAED) and crystallographic analysis, the major phase of hexagonal $\text{Mg}_4\text{Nb}_2\text{O}_9$ (Figs. 4.9 (b) and 4.10 (b)) and minor phase of MgNb_2O_6 nanoparticles in orthorhombic form were identified (Figs. 4.9 (c) and 4.10 (c)), in good agreement with the XRD results. In general, EDX analysis using a 20 nm probe from a large number of particles of the two calcined powders confirmed the parent composition to be $\text{Mg}_4\text{Nb}_2\text{O}_9$ (Fig. 4.11 (a)). Minor phase of MgNb_2O_6 was also confirmed by this technique, as illustrated in Fig. 4.11 (b). It is interesting to note that limited evidence for the presence of the unreacted starting precursor MgO (Fig. 4.12 (a) the ring patterns indicating the polycrystalline nature and hence fine scale of this phase Fig. 4.12 (b)) in good agreement with the SEM results, and nano-scale particle of MgNb_2O_6 was also found

in the TEM-EDX investigation, even though this could not be detected by XRD. It is, therefore, intriguing to note the advantage of a combination between TEM and EDX techniques, which lies in its ability to reveal microstructural features often missed by the XRD diffraction method which requires at least 5 wt.% of the component [138].



ลิขสิทธิ์มหาวิทยาลัยเชียงใหม่

Copyright© by Chiang Mai University

All rights reserved

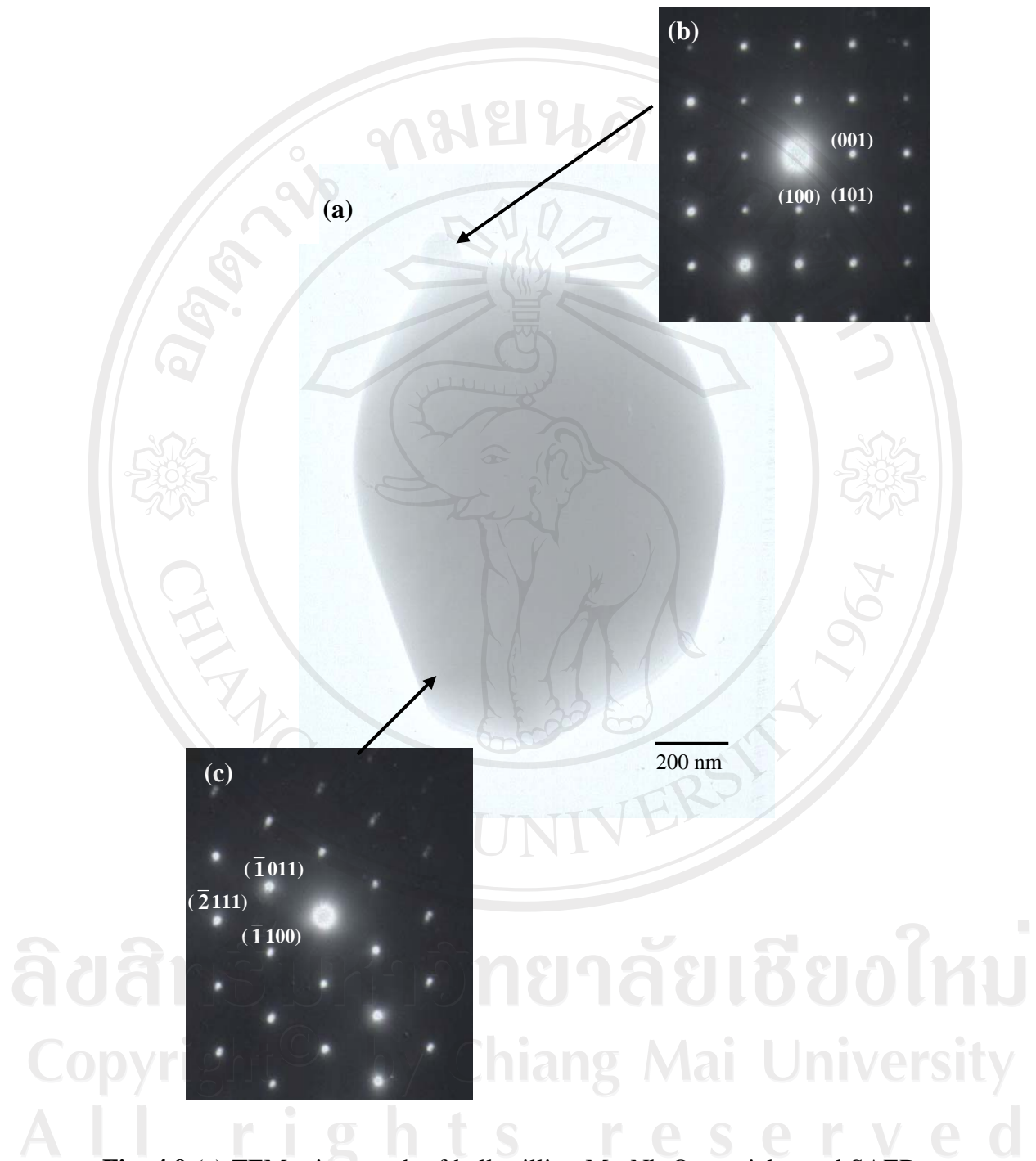


Fig. 4.9 (a) TEM micrograph of ball-milling $\text{Mg}_4\text{Nb}_2\text{O}_9$ particles and SAED patterns of (b) the major phase of hexagonal $\text{Mg}_4\text{Nb}_2\text{O}_9$ (zone axes $[111]$) and (c) the minor phase of orthorhombic MgNb_2O_6 (zone axes $[010]$).

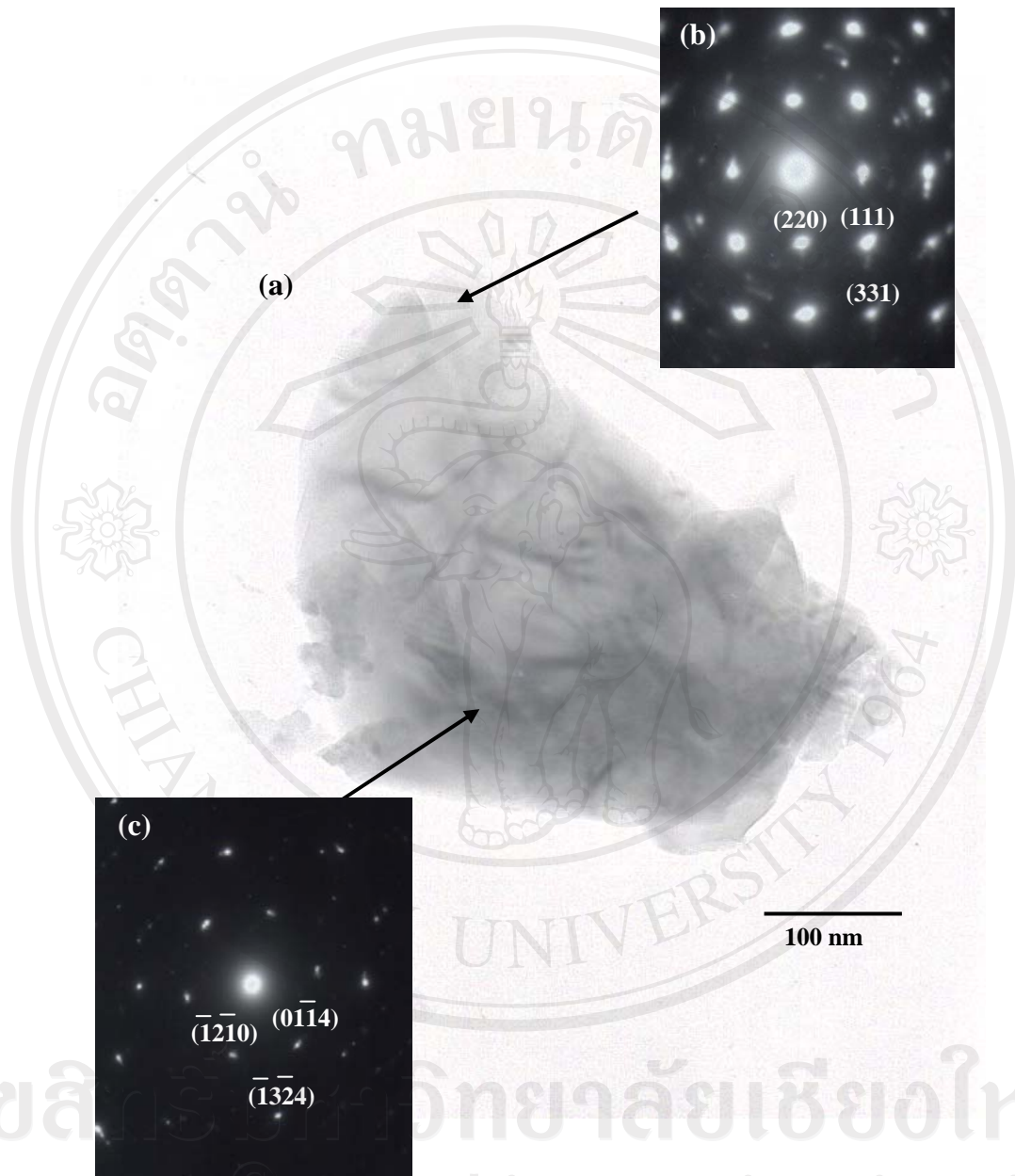
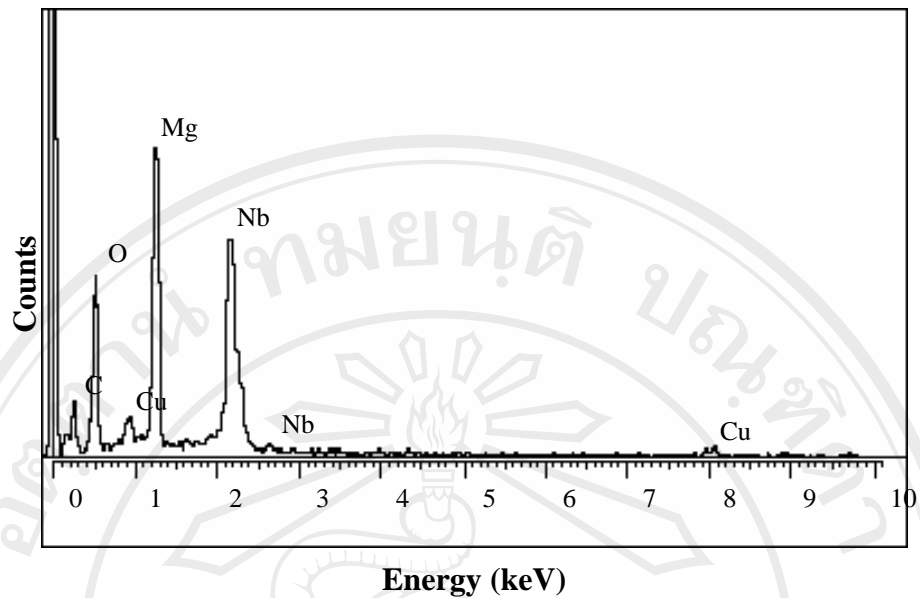
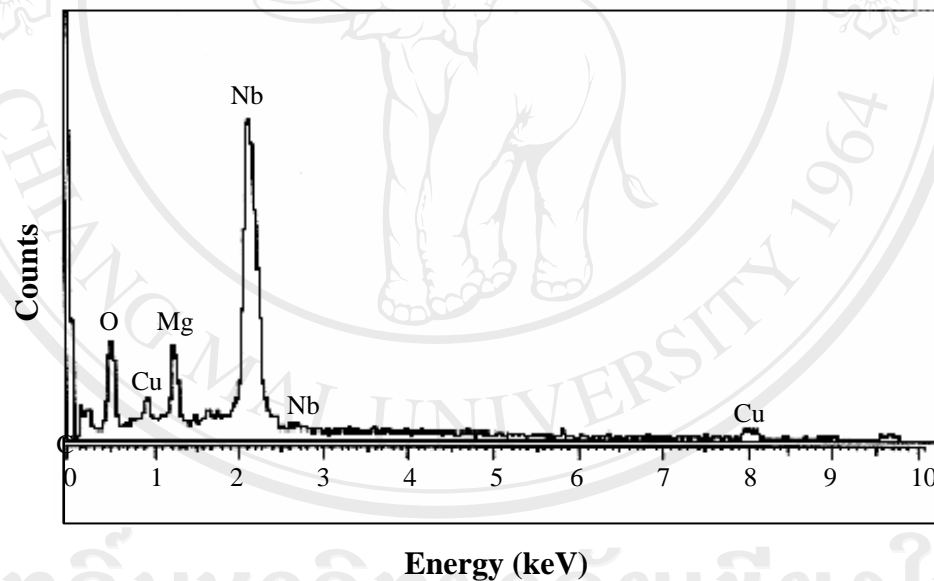


Fig. 4.10 (a) TEM micrograph vibro-milling of $\text{Mg}_4\text{Nb}_2\text{O}_9$ particles and SAED patterns of (b) the major phase of hexagonal $\text{Mg}_4\text{Nb}_2\text{O}_9$ (zone axes $[\bar{8}\bar{4}1]$) and (c) the minor phase of orthorhombic MgNb_2O_6 (zone axes $[001]$).

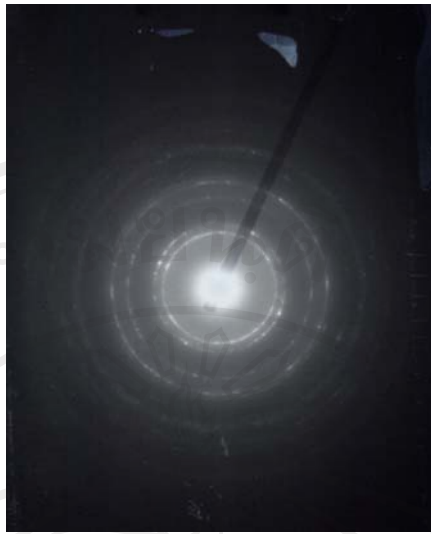


(a)

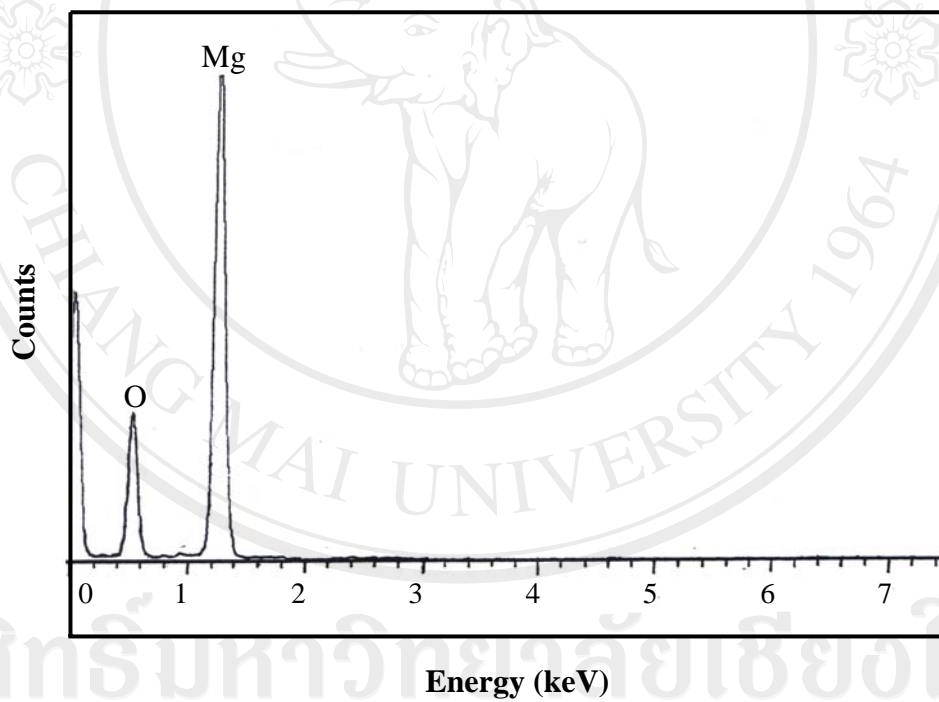


(b)

Fig. 4.11 EDX analysis of (a) the major phase $Mg_4Nb_2O_9$ and (b) the minor phase $MgNb_2O_6$ (some spectra indexed as C and Cu come from coated electrode and sample stub).



(a)



(b)

Fig. 4.12 (a) SAED pattern of the unreacted MgO phase and (b) EDX analysis of the MgO-rich phase.

4.2 Lead Magnesium Niobate Powders

Since the preparation of PMN using $\text{Mg}_4\text{Nb}_2\text{O}_9$ precursor has not been extensive as that of PMN using MgNb_2O_6 precursor. Moreover, its effect on the formation of perovskite PMN phase under various calcination conditions (especially the effects of applied dwell time and heating/cooling rates) has not been adequately characterized. Thus, the purpose of this section was to compare the two *B*-site precursor synthetic routes of PMN formation and the characteristics of the resulting powders. The phase formation, morphology and particle size of PMN has been investigated as a function of calcination conditions by TG-DTA, XRD, SEM and TEM techniques.

TG and DTA results for the mixtures synthesized by both *B*-site precursor methods (see section 3.1.1.1) are shown in Figs. 4.13 and 4.14, respectively. In general, similar trend of thermal characteristics is observed in both precursors. As shown in Fig. 4.13, the powders prepared via both *B*-site precursor mixed oxide methods demonstrate three distinct weight losses. The first weight loss occurs below 200 °C, the second one between 200-300 °C and the final one after 750 °C. In the temperature range from room temperature to ~ 150 °C, both samples show small thermal peaks in the DTA curves, Fig. 4.14, which are related to the first weight loss. These DTA peaks can be attributed to the decomposition of the organic species such as rubber lining from the milling process similar to our earlier reports [151,158]. In comparison between the two *B*-site precursor routes, after the first weight loss, the columbite-route shows a slightly higher weight loss over the temperature range of ~ 50-220 °C, followed by a much sharper fall in specimen weight with increasing

temperature from ~ 250 to 350 °C. This columbite-precursor method also exhibits larger overall weight loss (~ 1%) than that of the corundum route (~ 0.75%).

Corresponding to the second fall in specimen weight, by increasing the temperature up to ~ 700 °C, the solid-state reaction occurs between oxide precursors. The broad exothermic characteristic in both DTA curves represents that reaction, which has a maximum at ~ 600 and 800 °C for columbite- and corundum-routes, respectively. However, it is to be noted that there is no obvious interpretation of these peaks, although it is likely to correspond to a phase transition reported by a number of workers [28,40]. The different temperature, intensities and shapes of the thermal peaks for the two precursors here probably are related to the different starting materials especially magnesium niobate and consequently, caused by the removal of species differently bonded in the network, reactivity of different species (difference in type and dispersion of MgO) in the powders. These data were used to define the range of temperatures for XRD investigation between 550 and 1000 °C. It is to be noted that a significant weight loss in TG curves associated with large thermal change in DTA curves observed at temperatures above 750 °C (Figs. 4.13 and 4.14) may be attributed to the PbO volatilization typically found in lead-based ferroelectrics, consistent with other investigators [159,160].

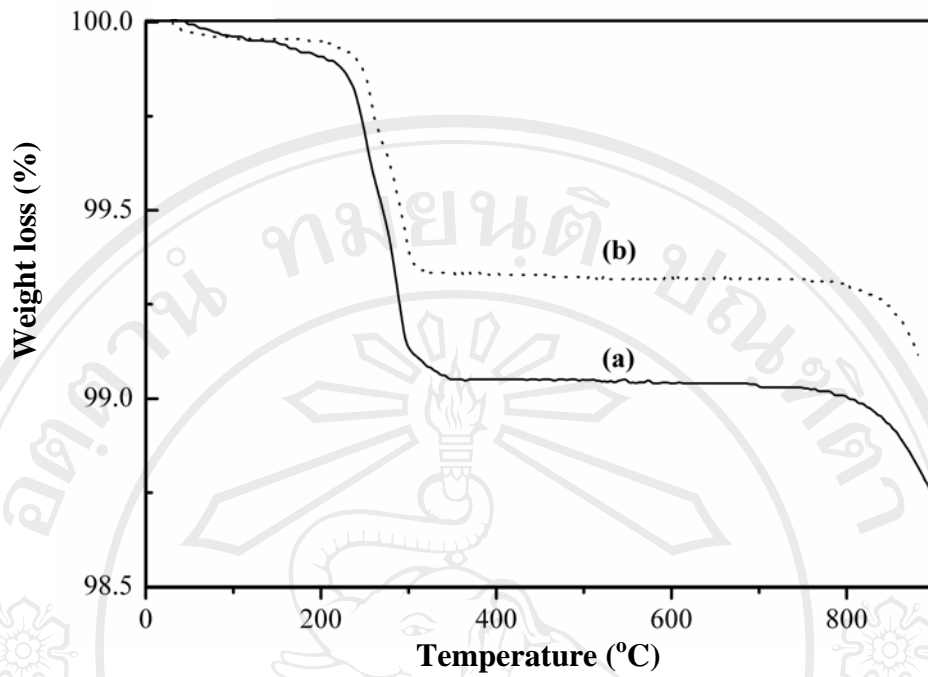


Fig. 4.13 TG curves of the mixtures derived from (a) columbite- and (b) corundum-routes.

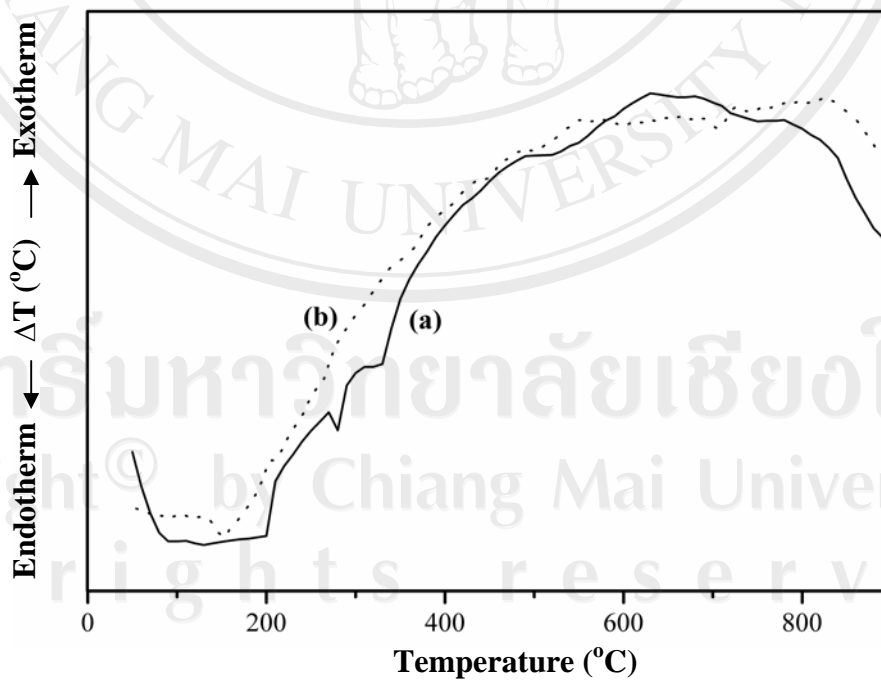


Fig. 4.14 DTA curves of the mixtures derived from (a) columbite- and (b) corundum-routes.

To study the phase development with increasing calcination temperature in each synthetic route, they were calcined at various temperatures for 1 h in air with constant heating/cooling rates of 10 °C/min, followed by phase analysis using XRD technique. As shown in Fig. 4.15, for the uncalcined powder and the powder calcined at 550 °C (columbite-route), only X-ray peaks of PbO and MgNb₂O₆ precursors are present. Similarly, it is seen that unreacted precursors of PbO and Mg₄Nb₂O₉ are detected from the original mixture up to 650 °C for the corundum-route (Fig. 4.16). These observations indicate that no reaction was yet triggered during the vibro-milling or low firing processes, in agreement with literature [40,151,158]. It is seen that PMN crystallites were developed in the powder at a calcination temperature as low as 600 and 650 °C for columbite- and corundum-routes, respectively. The results of X-ray diffraction measurement supported the DTA observation (Fig. 4.14) that PMN phase is formed at approximately 600-800 °C.

In general, the strongest reflections apparent in the majority of these XRD patterns indicate the formation of the lead magnesium niobate, PMN (∇). These can be matched with JCPDS file number 81-861 for the cubic phase, in space group $Pm\bar{3}m$ (no. 221) with cell parameters $a = 4.04 \text{ \AA}$ [161] consistent with other workers [40,162]. According to Fig. 4.15, the formation of Pb₃Nb₄O₁₃ (*) earlier reported by many researchers [40-42] has been found at 600 °C, which is associated to the second TG-DTA response in Figs. 4.13 and 4.14. This pyrochlore phase has a cubic structure with cell parameter $a = 10.56 \text{ \AA}$ in space group $Fd\bar{3}m$ (no. 227) (JCPDS file no. 25-443) [163]. Upon calcination at 650 °C, the peak corresponding to PbO disappeared (not detectable by XRD). By increasing the calcination temperature from 650 to 850

°C, the yield of the cubic PMN phase increases significantly until at 900 °C, a single-phase of perovskite PMN is formed for the columbite-route.

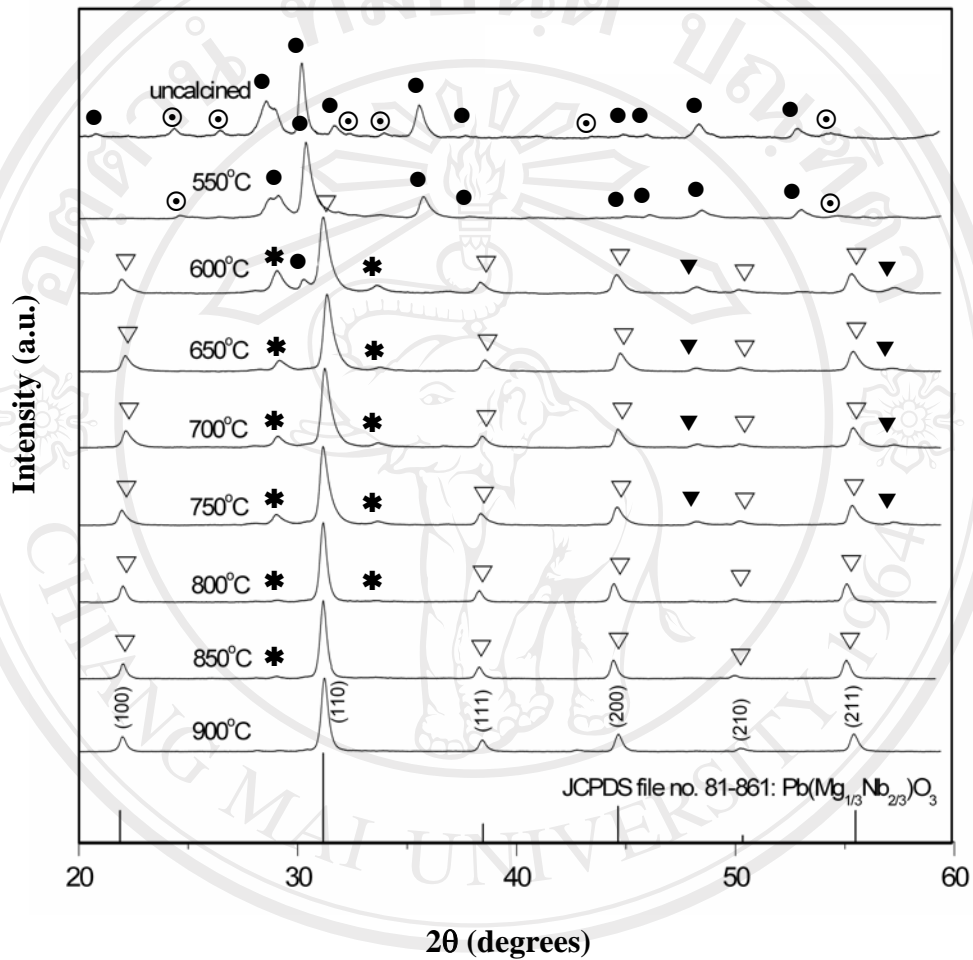


Fig. 4.15 XRD patterns of the columbite-route powders calcined at various conditions for 1 h with constant heating/cooling rates of 10 °C/min (● PbO, ⊙ MgNb₂O₆, * Pb₃Nb₄O₁₃ and ∇ Pb(Mg_{1/3}Nb_{2/3})O₃).

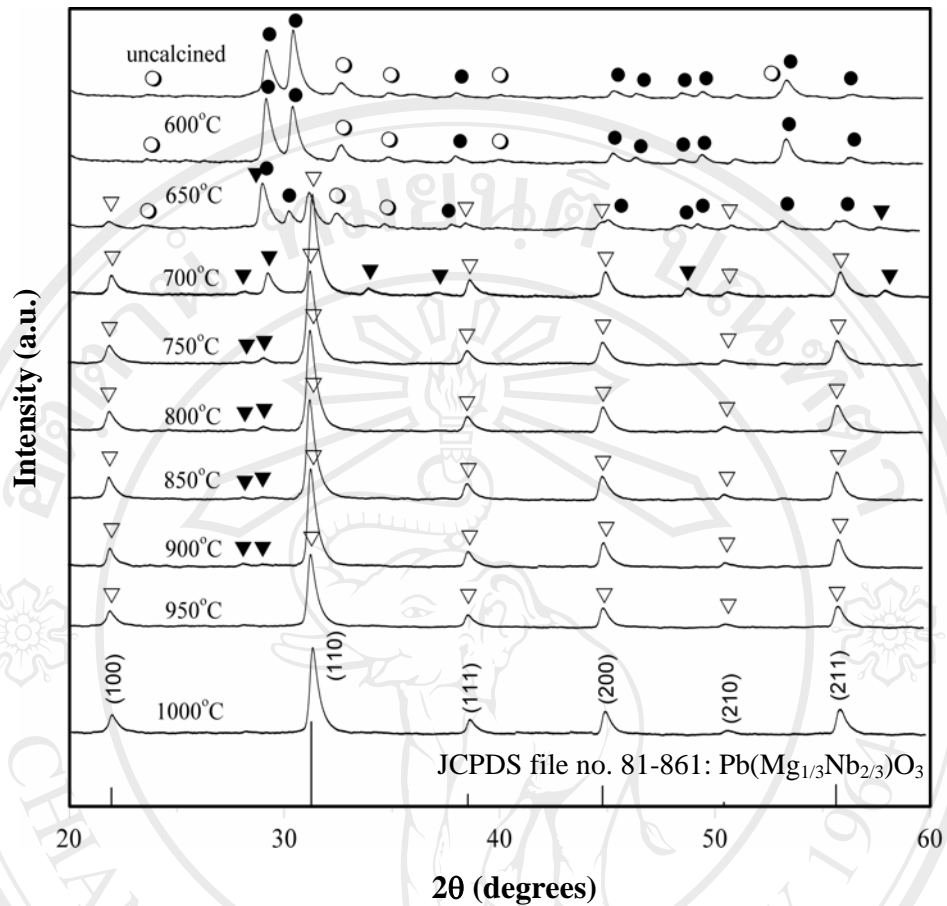


Fig. 4.16 XRD patterns of the corundum-route powders calcined at various conditions for 1 h with constant heating/cooling rates of 10 °C/min. (● PbO, ○ $\text{Mg}_4\text{Nb}_2\text{O}_9$, ▼ $\text{Pb}_{1.86}(\text{Mg}_{0.24}\text{Nb}_{1.76})\text{O}_{6.5}$ and ▽ $\text{Pb}(\text{Mg}_{1/3}\text{Nb}_{2/3})\text{O}_3$).

From Fig. 4.16, it is seen that calcination at 600 °C resulted in some new peak (▼) of the $\text{Pb}_{1.86}(\text{Mg}_{0.24}\text{Nb}_{1.76})\text{O}_{6.5}$ phase (JCPDS file no. 82-338) [164] mixing with the unreacted PbO and $\text{Mg}_4\text{Nb}_2\text{O}_9$ phases. To a first approximation, this $\text{Pb}_{1.86}(\text{Mg}_{0.24}\text{Nb}_{1.76})\text{O}_{6.5}$ phase earlier reported by many researchers [165,166] has a pyrochlore-type structure with a cubic unit cell $a = 10.60 \text{ \AA}$, space group $Fd3m$ (no. 227). This pyrochlore phase was found at 600 °C and totally disappeared at 950 °C. As the temperature increased to 900 °C, the intensity of the PMN peaks was further enhanced and PMN becomes the predominant phase, in good agreement with the earlier TG-DTA results. This study also shows that PMN is the only detectable phase in the corundum-route powders after calcination in the range 950-1000 °C.

In the present study, an attempt was also made to calcine both precursors under various dwell times and heating/cooling rates (Figs. 4.17 and 4.18). In this connection, it is seen that the single-phase of PMN (yield of 100% within the limitation of the XRD technique) was also found to be possible in columbite-precursor powders calcined at 850 °C for 3 h with heating/cooling rates as fast as 30 °C/min (Fig. 4.17). The appearance of Nb_2O_5 and $\text{Pb}_3\text{Nb}_4\text{O}_{13}$ phases indicated that chemical decomposition probably caused by PbO volatilisation has occurred at relatively high firing temperatures ($> 850 \text{ °C}$) with long dwell times, consistent with other workers [28,40,162]. It is also interesting to note that in this work the effects of both dwell time and heating/cooling rates were also found to be significant for the formation of perovskite PMN by using a corundum route (Fig. 4.18). It is seen that single-phase of PMN powders was also successfully obtained for a calcination temperature of 950 °C for 1 h with heating/cooling rates of 20 or 30 °C/min applied. The observation that the dwell time or heating/cooling rates may also play an

important role in obtaining a single-phase of lead-based perovskite ferroelectrics is also consistent with other investigators [40,64]. However, some additional peaks at $2\theta \sim 43^\circ$ are found in the Figs. 4.17 (a) and 4.18 (a). It is to be noted that there is no obvious interpretation of these peaks, although it is likely to correspond to a trace of MgO precursor. Nonetheless, with the limitation of X-ray technique and the inherent only single peak with very low intensity comparable to noise originated from the diffractometer, an accurate evaluation of the phase is not possible [138].

It is well established that the perovskite-type PMN tends to form together with the pyrochlore-type $\text{PbO-Nb}_2\text{O}_5$ compounds, depending on calcination conditions [28,164]. In the work reported here, evidence for the formation of PMN phase, which coexists with the cubic pyrochlore phase, is found after calcination at temperature $\sim 650\text{-}900^\circ\text{C}$, in agreement with literature [28,33,40]. No evidence of $\text{Pb}_{1.83}\text{Mg}_{0.29}\text{Nb}_{1.71}\text{O}_{6.39}$ was found, nor was there any indication of the pyrochlore phase of $\text{Pb}_3\text{Nb}_2\text{O}_8$ and $\text{Pb}_5\text{Nb}_4\text{O}_{15}$ [165,167] being present. In general, the formation temperature and dwell times for high purity PMN observed in the powders derived from a combination of a mixed oxide synthetic route and a carefully determined calcination condition (especially with a rapid vibro-milling technique) are slightly lower than those reported for the powders prepared via many other conventional mixed oxide methods [27,28,156].

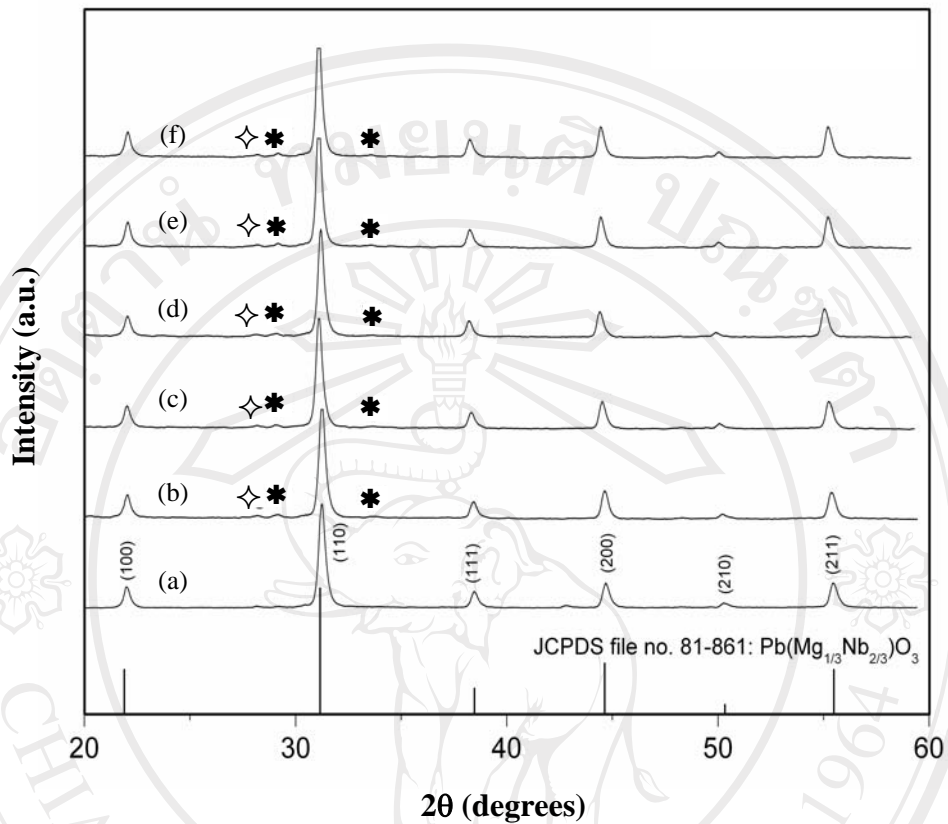


Fig. 4.17 XRD patterns of the columbite-route powders calcined at 850 °C, for 3 h with heating/cooling rates of (a) 30 °C/min, (b) 20 °C/min and (c) 10 °C/min, (d) for 2 h with heating/cooling rates of 10 °C/min and for 1 h with heating/cooling rates of (e) 30 °C/min and (f) 20 °C/min (◇ Nb_2O_5 and * $\text{Pb}_3\text{Nb}_4\text{O}_{13}$).

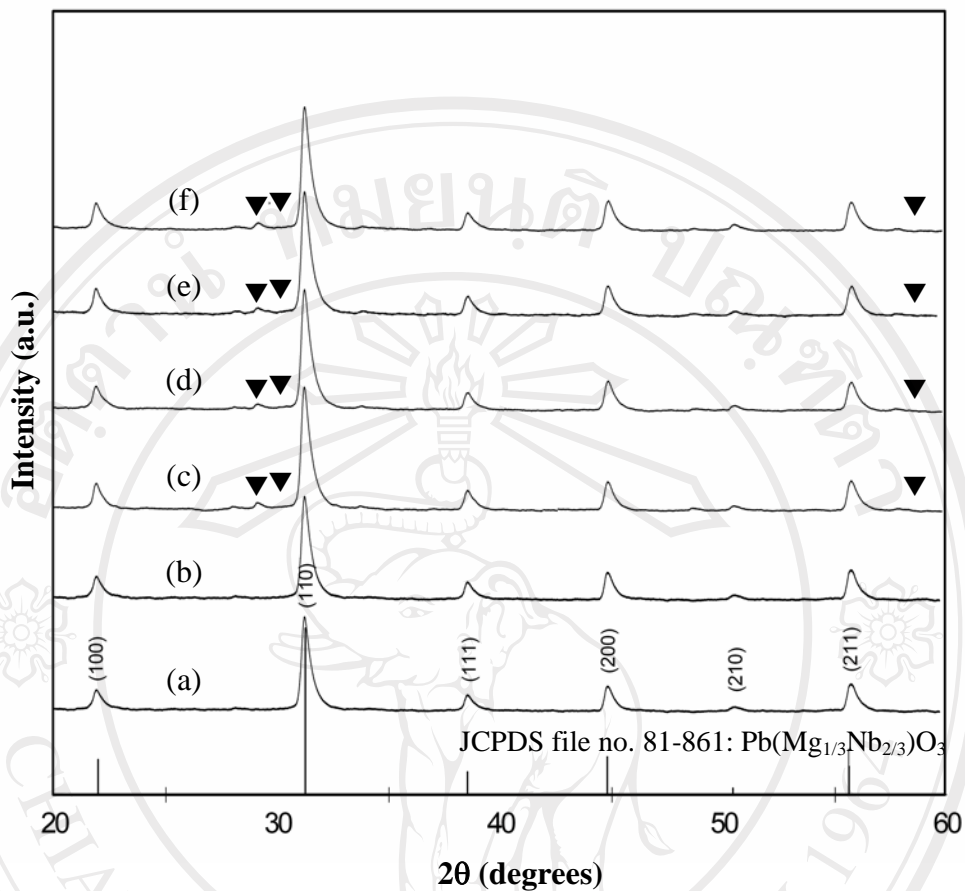


Fig. 4.18 XRD patterns of the corundum-route powders calcined at 950 °C for 1 h with heating/cooling rates of (a) 30 °C/min and (b) 20 °C/min, at 900 °C for (c) 2 h (d) 3 h and (e) 4 h, with heating/cooling rates of 10 °C/min, and (f) at 950 °C, for 4 h with heating/cooling rates of 30 °C/min (▼ $\text{Pb}_{1.86}(\text{Mg}_{0.24}\text{Nb}_{1.76})\text{O}_{6.5}$).

Based on the TG-DTA and XRD data, it may be concluded that, over a wide range of calcination conditions, single-phase perovskite PMN cannot be straightforwardly formed via a two-step *B*-site precursor method, as verified by a number of researchers [28,40]. The experimental work carried out here suggests that the optimal calcination conditions for single-phase PMN are 900 °C for 1 h or 850 °C for 3 h (columbite-route) and 950 °C for 1 h (corundum-route), with heating/cooling rates as fast as 30 °C/min. The optimised formation temperature of single-phase PMN was lower for the columbite-route probably due to the higher degree of reactivity with less reacting species involved [28]. As suggested by several workers [165,166], the degree of cation mixing in precursors significantly affects the phase formation behavior in the *B*-site synthesis of PMN. This observation may be accounted for by the fact that the columbite route possibly provides faster chemical reaction rate (only the reaction between PbO and MgNb₂O₆) and is able to enhance the formation of perovskite PMN phase by increasing the reactivity of MgO [28]. However, the minimum firing temperature required for the manufacturing of single-phase corundum Mg₄Nb₂O₉ (~ 950 °C [142]) is lower than that of columbite MgNb₂O₆ (~ 1000 °C [151]).

Therefore, in general, the methodology presented in this work provides a simple method for preparing perovskite PMN powders via a solid-state mixed oxide synthetic route. It is interesting to note that, by using either columbite- or corundum-routes, with an optimal calcination condition, the reproducible, low cost and flexible process involving simple solid-state reaction synthetic route can produce high purity perovskite PMN (with impurities undetected by XRD technique) from relatively impure and inexpensive commercially available raw materials.

To further study the influence of precursor on the characteristics of the resulting PMN powders, a combination of particle size analysis, SEM, TEM and EDX is used to examine the powders obtained, as shown in Figs. 4.19-4.22 and Table 4.3. Fig. 4.19 compares the particle size distribution curves of calcined PMN powders derived from both *B*-site precursor methods, which indicate an appreciable size fractions at approximately 0.75-1.08 μm diameters, as also listed in Table 4.3 (averaged sizes). Even taking in account that the analysis does not reveal the real dimension of single particles (due to agglomeration effects as expected from the SEM results in Fig. 4.20), a uniform frequency distribution curve was observed for the columbite-route whilst narrow distribution curve with tiny kink at front covering the range of 0.32-1.65 μm in sizes was found for the corundum-route, reflecting more the size of agglomerates than the real size of particles.

Table 4.3 Particle size range of PMN particles measured by different techniques.

Measurement techniques	Particle size range (average)	
	Columbite-route	Corundum-route
XRD ^a (nm, ± 2.0)	26.60	22.50
Laser diffraction (μm , ± 0.2)	0.15-7.50 (1.08)	0.32-1.65 (0.75)
SEM (μm , ± 0.1)	0.25-3.00 (1.63)	0.20-1.25 (0.73)
TEM (μm , ± 0.01)	0.25-0.65 (0.45)	0.10-0.55 (0.33)

^a Crystallite size.

SEM micrographs of the calcined PMN powders derived from columbite- and corundum-precursor methods are shown in Fig. 4.20 (a) and (b), respectively. In general, the particles are agglomerated and basically irregular in shape, with a substantial variation in particle size. Observed diameters range from 0.25 to 3.00 μm and 0.20 to 1.25 μm for columbite- and corundum-routes, respectively, in good agreement with the particle size distribution previously determined (Table 4.3). The primary particles in the agglomerates are, however, submicron in size. This is confirmed by TEM micrographs shown in Figs. 4.21 and 4.22. Additionally, the observed morphology reveals considerable difference in homogeneity, uniformity, size and shape between the two PMN powders. It is obviously evident that the columbite-route powders exhibit more heterogeneous morphology than the corundum-route powders. The columbite-route powders consist mainly of irregular round shape primary particles with a diameter of $\sim 1 \mu\text{m}$ or less (Fig. 4.20 (a)). In addition to the primary particles, the powders have another kind of very fine particle (darker particles) with diameter of about 200 nm. A combination of SEM and EDX techniques has demonstrated that pyrochlore and unreacted precursor phases (marked as “y” and “z” in the micrograph in Fig. 4.20 (a)) exist neighbouring the parent PMN phase (marked as “x”) (see also Table 4.4). In general, EDX analysis using a 20 nm probe from a large number of particles of the two calcined powders confirmed the parent composition to be PMN. It is interesting to note that nano-scale MgO and PbO inclusions were also found in the SEM-EDX investigation for the columbite-route, in agreement with earlier works [29,143], even though this could not be detected by XRD. It is, therefore, intriguing to note the advantage of a combination between SEM

and EDX techniques, which lies in its ability to reveal microstructural features often missed by the XRD method which requires at least 5 wt% of the component [138].

However, it is seen that higher degree of agglomeration with more rounded particle morphology is observed in the powders produced by the corundum route (Fig. 4.20 (b)). The strong interparticle bond within each aggregate is evident by the formation of a well-established necking between neighbouring particles. This observation could be attributed to the mechanism of surface energy reduction of the ultrafine powders, i.e. the smaller the powder the higher the specific surface area [144]. In general, it is seen that primary particle in corundum-route powders is clearly smaller in size than the columbite-route powders. The averaged particle size of corundum-precursor PMN powders with finer particle size is regarded as advantage for better reactivity.

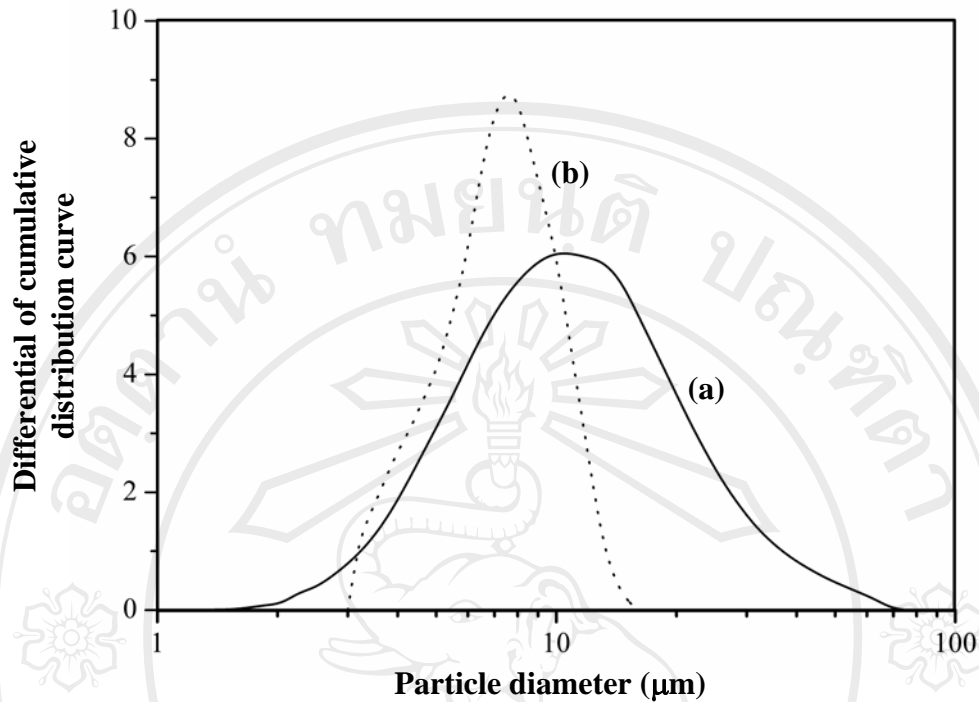
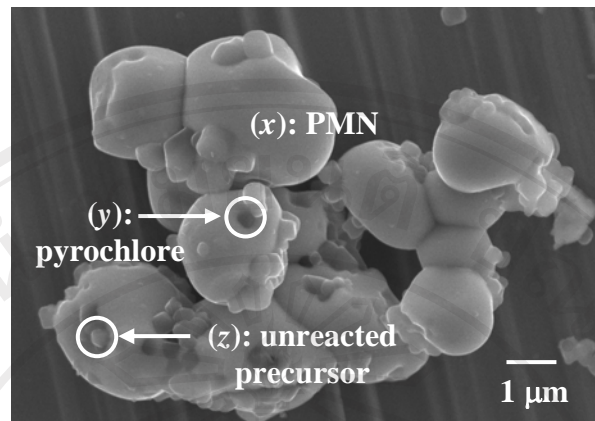
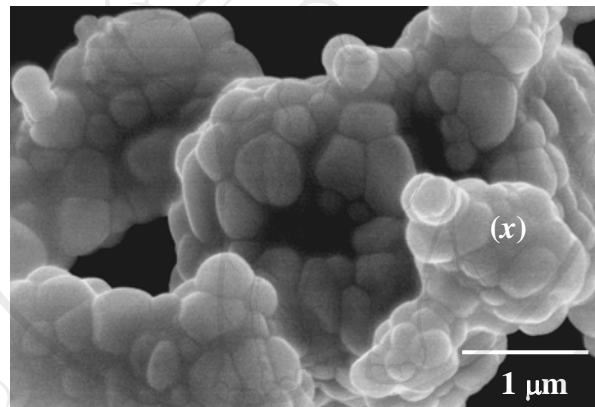


Fig. 4.19 The particle size curves of (a) the columbite- and (b) corundum-route PMN powders after calcined at their optimised conditions.



(a)



(b)

Fig. 4.20 SEM micrographs of the: (a) columbite- and (b) corundum-route PMN powders after calcined at their optimised conditions.

Bright field TEM images of discrete particles of the calcined PMN powders are shown in Figs. 4.21 (a) and 4.22 (a) for the columbite- and corundum-routes, respectively, indicating the particle sizes and shapes at higher magnifications. The observed morphology reveals the considerable difference in both size and shapes between the two particles. Primary particle in the columbite-route PMN powders is clearly larger in size and also higher in angularity than the corundum-route powders.

By employing a combination of both selected area electron diffraction (SAED) and crystallographic analysis, the perovskite phase of cubic PMN was identified for the columbite- and corundum-routes as shown in Figs. 4.21 (b) and (c) and 4.22 (b) and (c), respectively, in good agreement with the XRD results.

It has been shown that single-phase perovskite PMN powders can be successfully formed by employing either columbite or corundum *B*-site precursor method via a rapid vibro-milling. Evidence for the formation of a cubic pyrochlore phase, which coexists with the perovskite PMN parent phase, is found at calcination temperature ranging from 800 to 1050 °C. Amongst the two *B*-site precursor methods, it is seen that lower optimized calcination temperature for the production of pure PMN powders can be obtained by using the columbite-route, whereas the smallest obtainable particle size was found in the corundum-route PMN powders.

Although the single-phase perovskite PMN powders can be successfully synthesized by both *B*-site precursors. However, most of the published works [28,39,136], so far, has been concentrated on the use of PMN columbite-route powders to fabricate PMN ceramics. On the other hand, the preparation and characterization of PMN ceramics via corundum-route powders has not been widely investigated. Therefore, in the next sections, PMN corundum-route powders were used for the fabrication of PMN and PMN-PT ceramics.

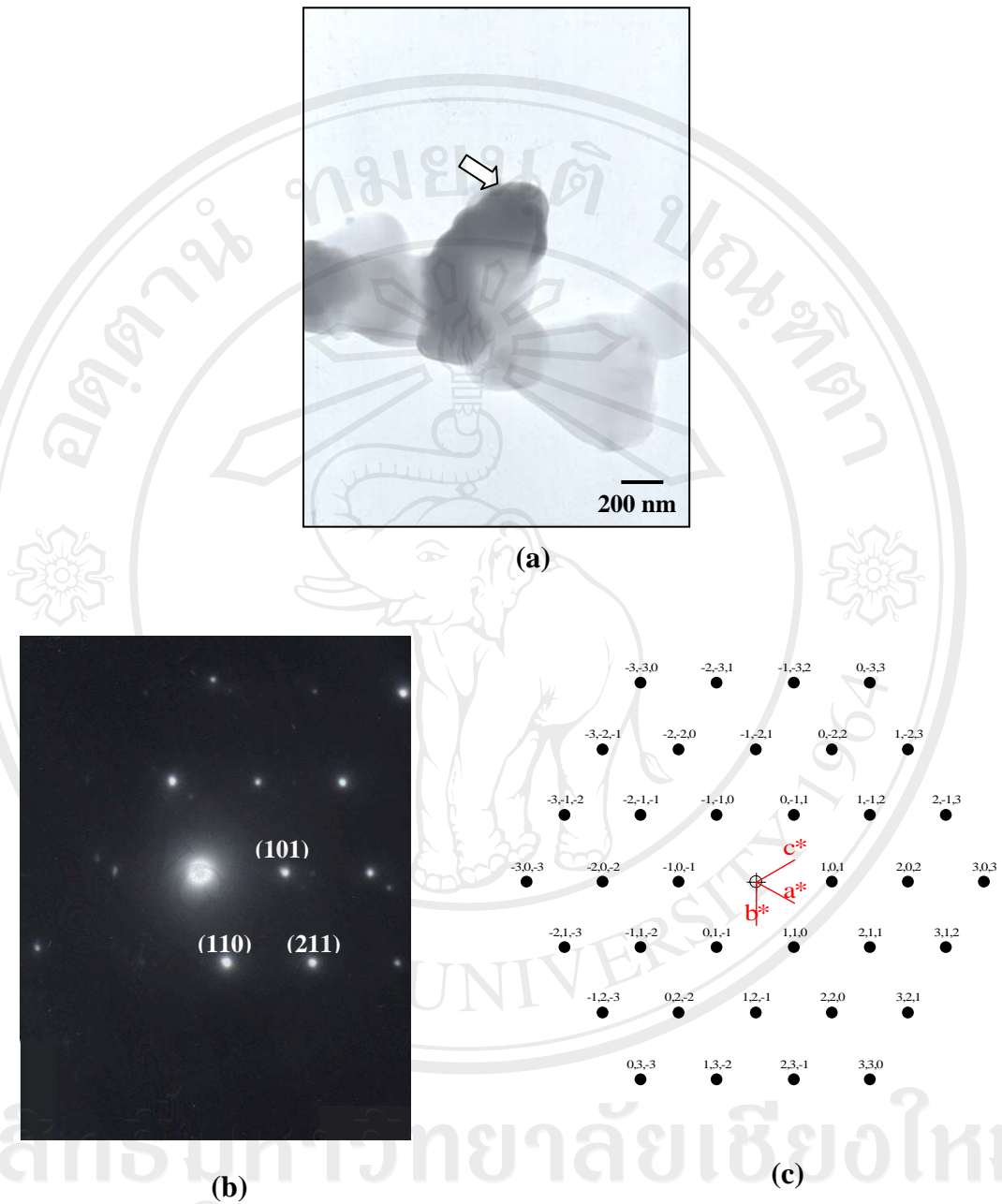


Fig. 4.22 (a) TEM micrograph with arrow indicates (b) SAED pattern ($[\bar{1}11]$ zone axes) and (c) reciprocal lattice pattern simulation of the corundum-route PMN particles.

4.3 Lead Magnesium Niobate Ceramics

Having prepared the single-phase PMN powders by using $Mg_4Nb_2O_9$ precursor, dense PMN ceramics were fabricated by sintering the PMN powders (calcined at 950 °C for 1 h with heating/cooling rates of 30 °C/min) at various temperatures for 2 h with heating/cooling rates of 5 °C/min [136]. As these PMN powders could be prepared in a reproducible manner attention has been focus on chemical composition, microstructure, thermal expansion and dielectric properties of the sintered PMN ceramics with maximum density.

X-ray diffraction patterns of the PMN ceramics sintered at various temperatures are displayed in Fig. 4.23, indicating the formation of both perovskite and impurity phases in each case. The strongest reflections in the majority of all XRD traces indicate the formation of the PMN perovskite phase, which could be matched with JCPDS file no. 81-861, in agreement with other works [40,162]. A pseudo-cubic perovskite-type structure with cell parameter $a = 4.04 \text{ \AA}$ was identified. Almost 100% perovskite phase PMN ceramics were obtained as shown in the XRD patterns of polished surfaces of pellets. It should be noted that no evidence of pyrochlore phases such as $Pb_2Nb_2O_7$, $Pb_3Nb_2O_8$ and $Pb_5Nb_4O_{15}$ reported by other worker [25,28,43] has been formed here. The relative amounts of perovskite phase and relative densities present in each sintered ceramic were calculated from Eqs. (3.7) and (3.12) (numerical data are presented in Table 4.4).

Table 4.4 Physical properties of singly sintered PMN ceramics.

Sintering temperature (°C)	Perovskite phase (%)	Relative ^a density (%)	Shrinkage ^b (%)	Weight loss ^c (%)
1100	100	63.2	2.54	1.1
1150	100	70.5	5.74	2.5
1200	100	85.1	8.77	4.6
1250	100	89.3	9.63	4.8

^a The estimated precision of the density is $\pm 0.1\%$.

^b The estimated precision of the shrinkage is $\pm 0.05\%$.

^c The estimated precision of the weight loss is $\pm 0.1\%$.

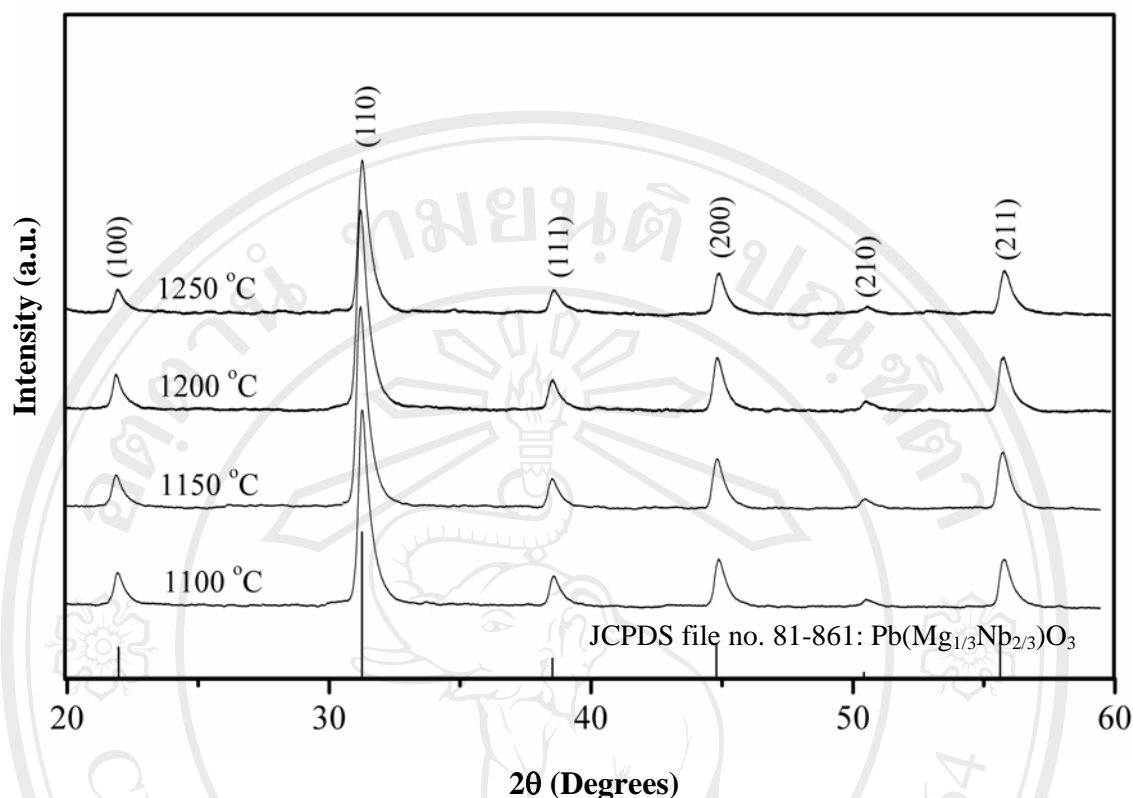


Fig. 4.23 XRD patterns of PMN ceramics sintered at various temperatures.

The theoretical density of cubic phase of PMN ceramics, which was used for the relative density calculations in the sintered samples, was estimated from the lattice parameter data to be $\sim 8.116 \text{ g/cm}^3$ (JCPDS file no. 81-861) [161]. Densities of the sintered samples were determined by using Archimedes principle. Density, shrinkage and weight loss data of all PMN ceramics sintered at various temperatures are given in Table 4.4. It is observed that a density of about 63-89% of the maximum value for PMN can be achieved in this study. The maximum density was obtained only in the samples sintered at 1250°C for 2 h, in good agreement with the study by Liou *et al.* [136] with heating/cooling rates of $5^\circ\text{C}/\text{min}$. Density increases as sintering temperature increase from 1100°C h to 1250°C . For shrinkage measurement, it is

seen that the change in dimension was rapidly increased with sintering temperature at 1100 °C to 1200 °C and nearly constant after 1250 °C. Weight losses of all PMN ceramics during sintering procedure can be thought of as a measure of the degree of PbO volatilization. This was analyzed by recording the weight before and after sintering procedure. In general, the weight loss increases with sintering temperature.

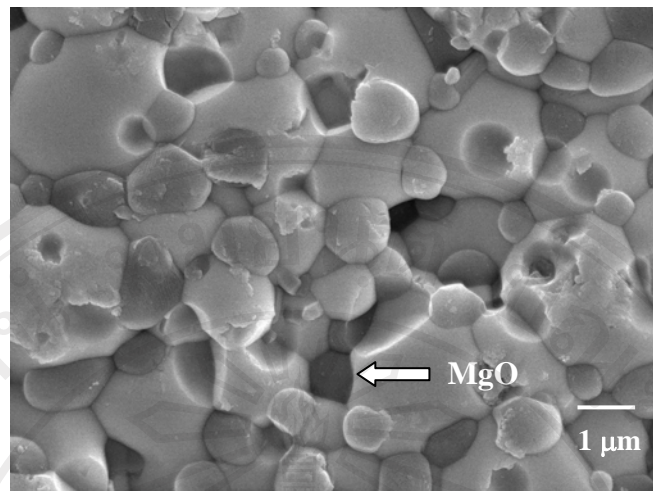
Microstructural development of sintered PMN ceramic with maximum bulk density was investigated by scanning electron microscopy (SEM). Micrographs of as-sintered and fracture surfaces of PMN ceramics sintered at 1250 °C for 2 h with heating/cooling rates of 5 °C/min are shown in Fig. 4.24 (a) and (b), respectively. In general, typical PMN microstructures consisting of highly dense grain-packing was observed in good agreement with previous works [29,107]. The as-sintered ceramics showed few pores at grain boundaries and triple points; cracks or microcracks were not detected. The grain sizes are in the range of 0.8-2.3 μm .

It was recognized that the XRD data alone could neither confirm nor rule out the presence of MgO because the high intensity XRD peak of MgO at $d_{200} = 2.106 \text{ \AA}$ is almost overlapped by the perovskite PMN peak at $d_{200} = 2.03 \text{ \AA}$ [165]. Nevertheless, the presence of MgO in specimens was confirmed by SEM/EDX analysis. In general, EDX analysis of PMN grains showed that the composition (at%) of Pb : Mg : Nb is 17.06 : 5.78 : 19.05. MgO inclusions correspond to dark particles, which can be found on the surfaces of some PMN grains as shown in Figs. 4.24 (a). Their corresponding EDX spectra are given in Fig. 4.25. It is to be note that the characteristic morphology of MgO dispersed in PMN grains is consistent with Guha [165]. On the other hand, micrograph of fracture surface (Fig. 4.24 (b)) exhibits highly dense microstructure consisting of equiaxed grains in good agreement with other researchers [4,29,107]. A

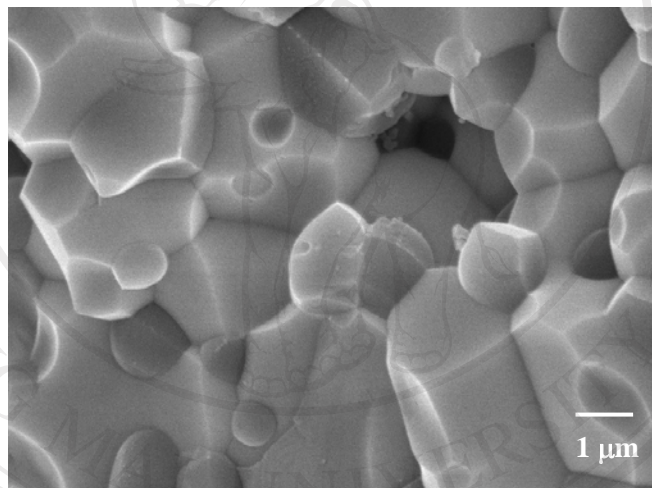
few amounts of small pores could be found in this bulk structure. The PMN ceramics also have an intergranular fracture mechanism indicated that the grain boundaries are mechanically weaker than the grains [168].



ลิขสิทธิ์มหาวิทยาลัยเชียงใหม่
Copyright© by Chiang Mai University
All rights reserved



(a)



(b)

Fig. 4.24 SEM micrographs of (a) as-sintered and (b) fracture surfaces for PMN ceramics with maximum bulk density.

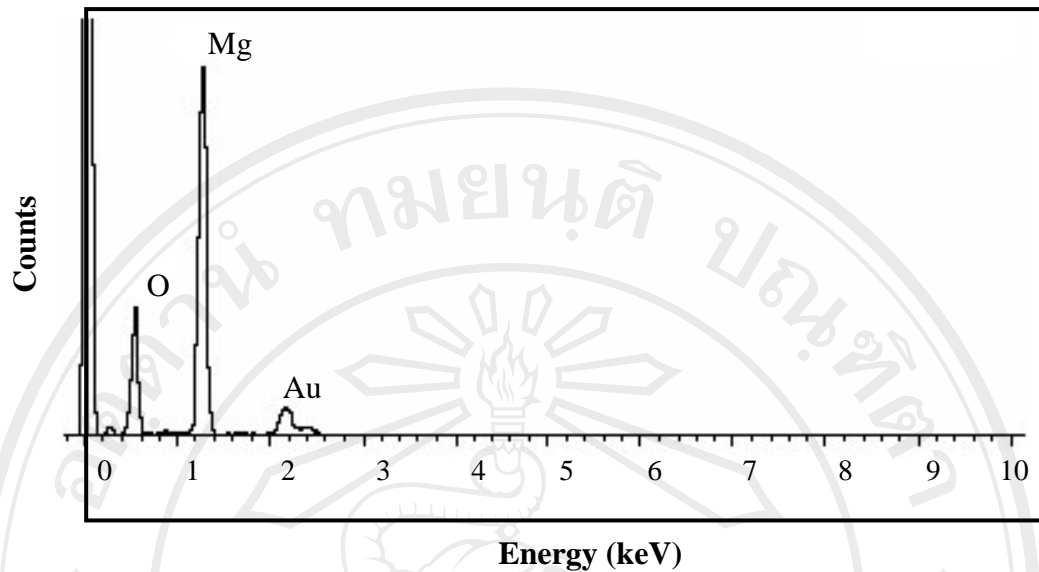


Fig. 4.25 Representative EDX spectra obtained from the dark particles (arrowed in Fig. 4.24 (a)) exist on the surface of PMN grains (some spectra indexed as Au come from coated electrode).

In order to evaluate the dielectric properties, the highest dense PMN sample was measured at frequencies between 1 kHz and 100 kHz in the temperature range from -50 to +50 °C as shown in Fig. 4.26. In general, the PMN sample exhibits a typical relaxor ferroelectric response, with temperatures of maximum dielectric constant, $T(\epsilon_{r,\max})$, of about -10 °C (1 kHz), in agreement with author works [167,169]. In this work, it is found that the maximum magnitude of both $\epsilon_{r,\max}$ and $\tan \delta_{\max}$ in PMN samples close to those observed in the typical columbite-route [35,136]. The maximum temperatures were found to decrease with increasing frequency. These observations are consistent with earlier work on other PMN-based systems [136,162].

The polarization (P - E) hysteresis loops of unpoled PMN ceramic which measured at $-100\text{ }^{\circ}\text{C}$ were illustrated in Fig. 4.27. In general, the PMN ceramic exhibits typical slim-shaped polarization-field hysteresis loop. The shape of P - E loops varies with the applying electric field (5-40 kV/cm). This behavior is more likely observed in conventionally sintered sample. Up to the equipment highest field (40 kV/cm), PMN show a slim type ferroelectric loop with 10.402 kV/cm of coercive field (E_C), $6.519\text{ }\mu\text{C}/\text{cm}^2$ of remnant polarization (P_r) and $12.498\text{ }\mu\text{C}/\text{cm}^2$ of saturate polarization (P_s). Additionally, small values of ferroelectric parameters (E_C , P_r , P_s) may be attributed to the fact that insufficient electric field was applied to the sample due to the limitation of measurement set-up.

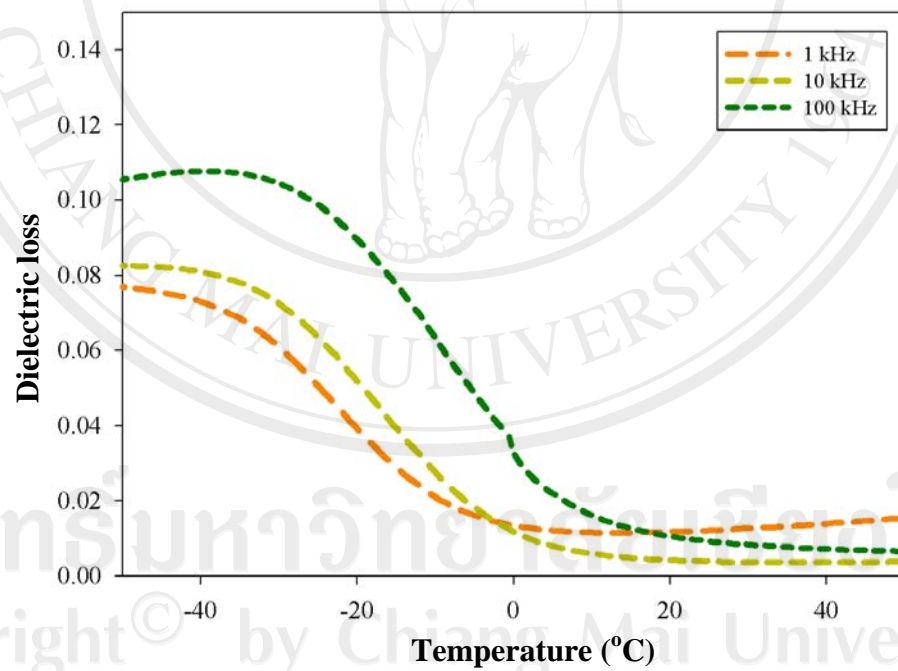
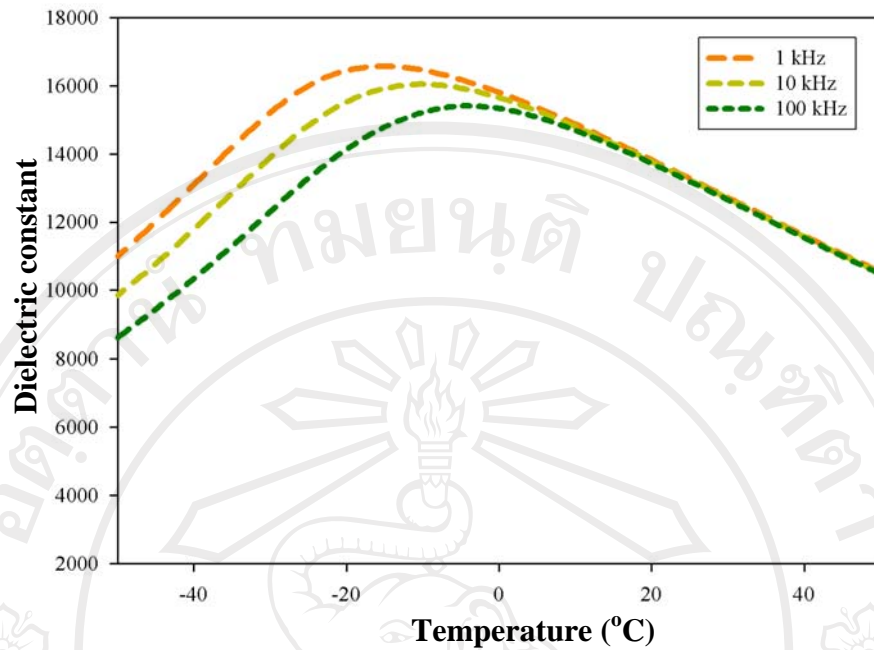


Fig. 4.26 (a) Dielectric constants (ϵ_r) and (b) dielectric loss ($\tan\delta$) response of the PMN ceramic.

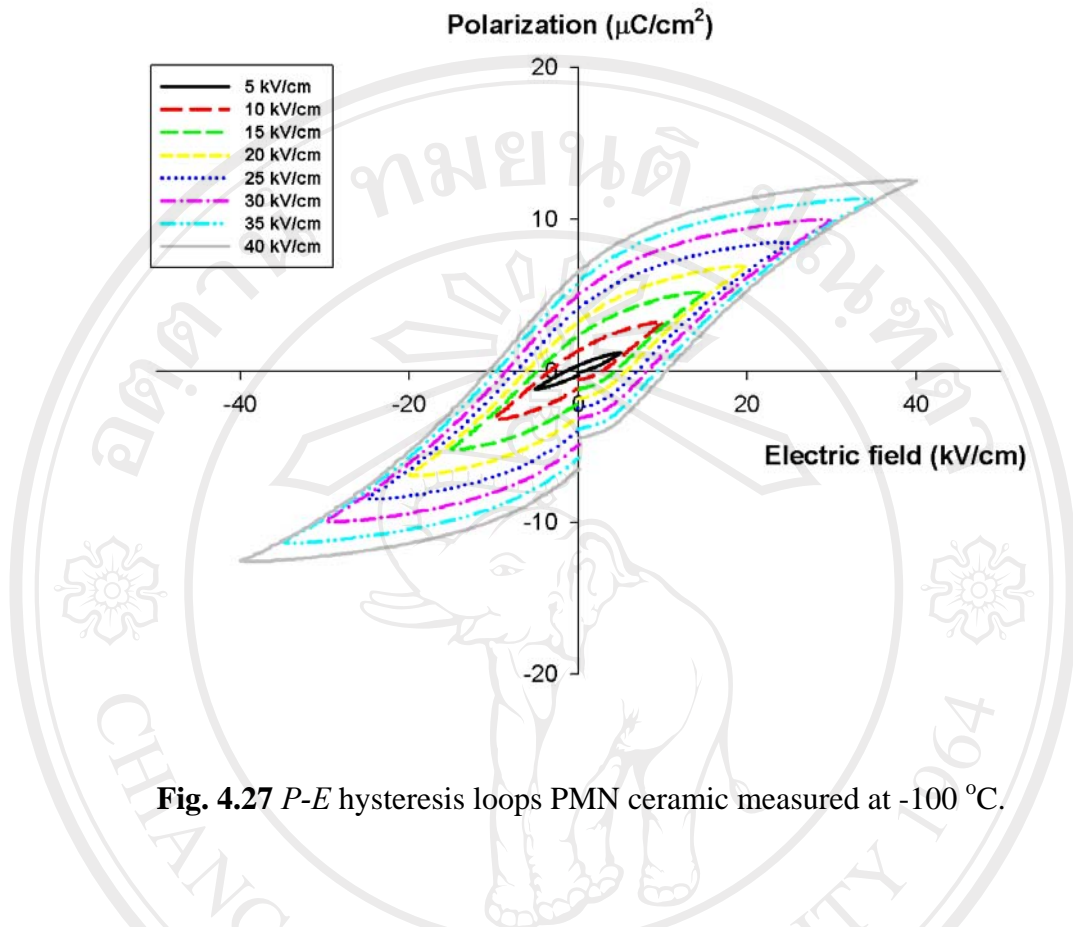


Fig. 4.27 *P-E* hysteresis loops PMN ceramic measured at $-100\text{ }^{\circ}\text{C}$.

The result of dilatometric measurement of PMN ceramic is presented in Fig. 4.28 (solid line is thermal expansion and dot line is thermal expansion coefficient). It can be noticed that the thermal expansion is very low with low thermal expansion coefficient near room temperature or near the Curie point. The temperature of the dielectric permittivity maximum, T_m of this ceramic occurs at around $-10\text{ }^{\circ}\text{C}$, in good agreement with the previously published values [35,169]. The value of thermal expansion coefficient in the temperature range of $-100\text{ }^{\circ}\text{C}$ to $100\text{ }^{\circ}\text{C}$, as determined from heating cycle for PMN is $1.6 \times 10^{-6}\text{ }^{\circ}\text{C}^{-1}$.

On analyzing the deviation of the strain from the high-temperature linear behavior, P_d values can be obtained at various temperatures. From the phenomenological approach we know that the P_S values can be extracted by using the Eq. 3.8. Using the values of $Q_{11} = 0.123 \times 10^{-2} \text{ m}^4/\text{C}^2$ and $Q_{12} = -0.049 \times 10^{-2} \text{ m}^4/\text{C}^2$ [170], P_d values can be calculated, as plotted in Fig. 4.29. When calculating the spontaneous strains of the rhombohedral at a particular temperature, the cubic cell constant should be extrapolated to that temperature accounting for the thermal expansion. A linear extrapolation from above the transition temperature can be made over a narrow range with fairly good accuracy. In Fig. 4.29, we calculated the $P_d \sim ((P_d^2)^{1/2})$ from $\Delta l/l$. The normal reversible polarization data, P_r , determined from the P - E measurements is also plotted. It is evident that the polarization calculated from the strain is larger than P_r and extend several hundred degrees above T_C due to quadratic electrostrictive effects. Moreover, for temperatures well below T_C , although not equal, P_d and P_r are comparable even they are obtained by totally independent techniques.

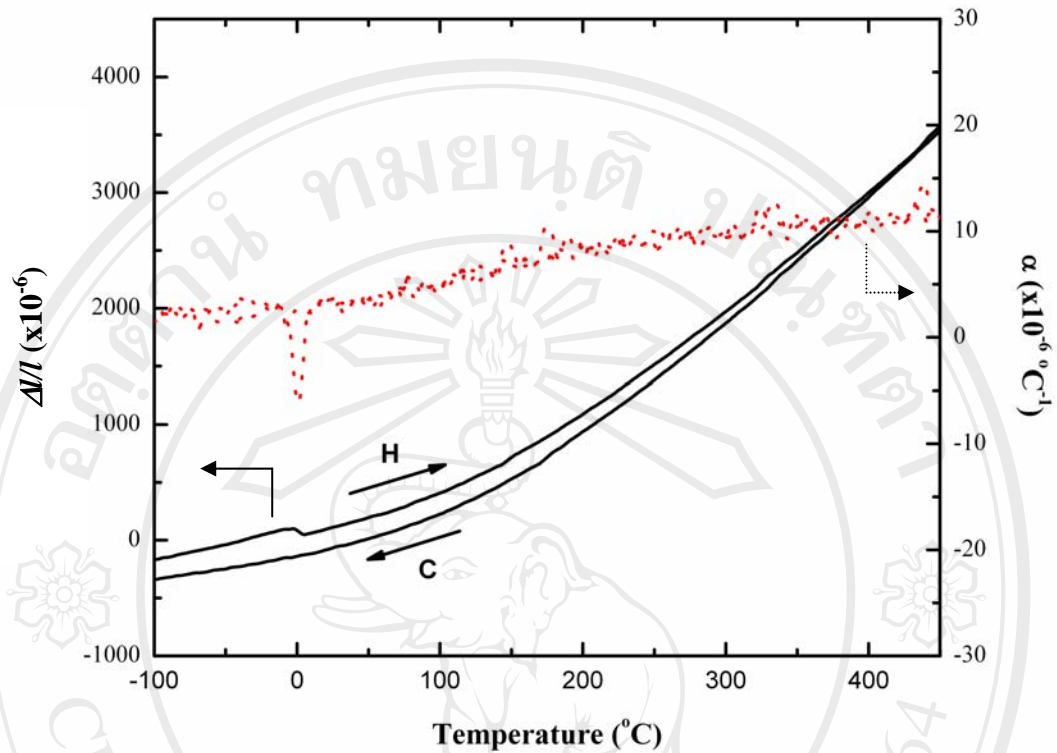


Fig. 4.28 Thermal expansion ($\Delta l/l$) and thermal expansion coefficient (α) as a function of temperature for pure PMN ceramics (H = heating cycle and C = cooling cycle).

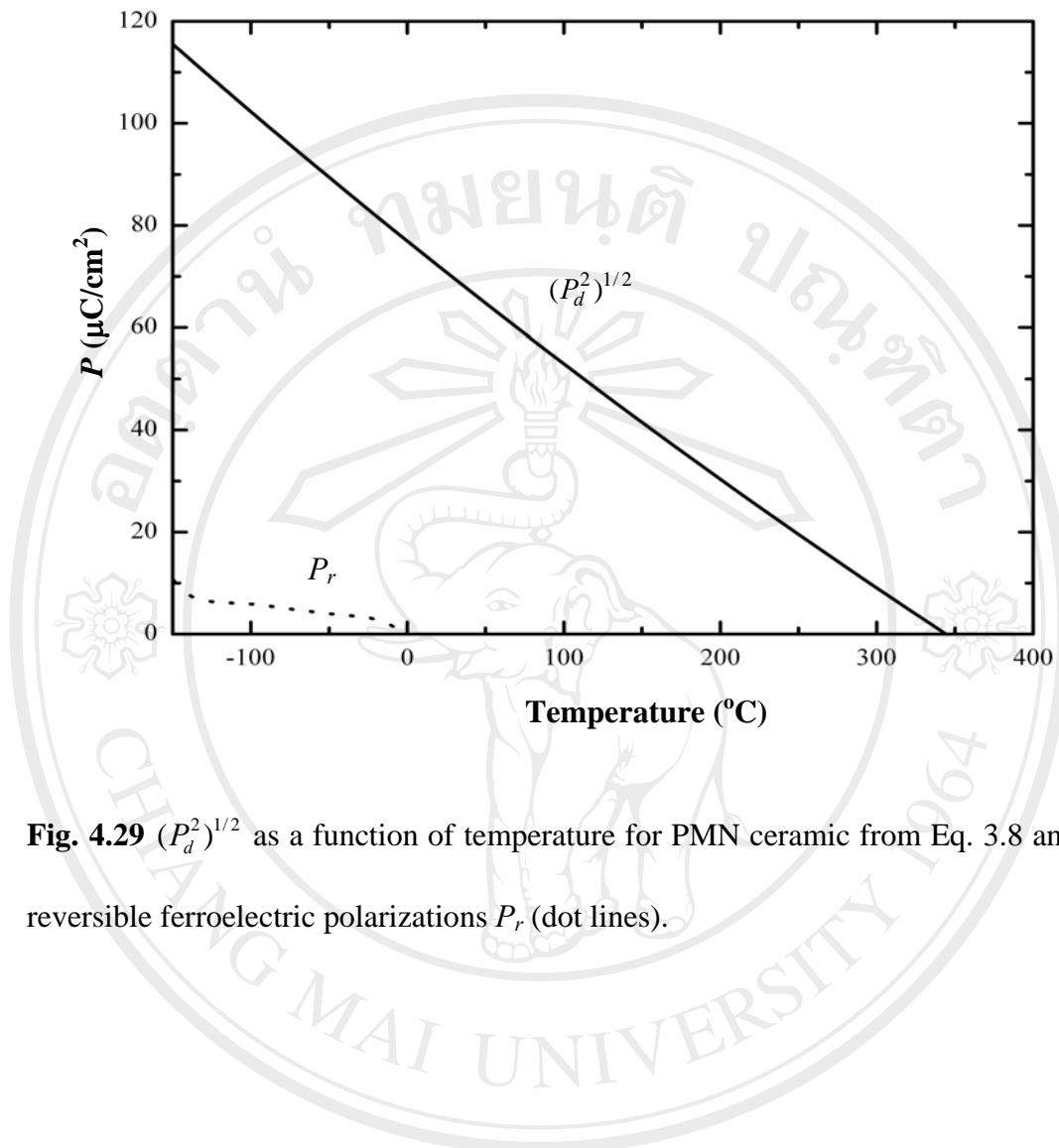


Fig. 4.29 $(P_d^2)^{1/2}$ as a function of temperature for PMN ceramic from Eq. 3.8 and the reversible ferroelectric polarizations P_r (dot lines).